Accepted Manuscript

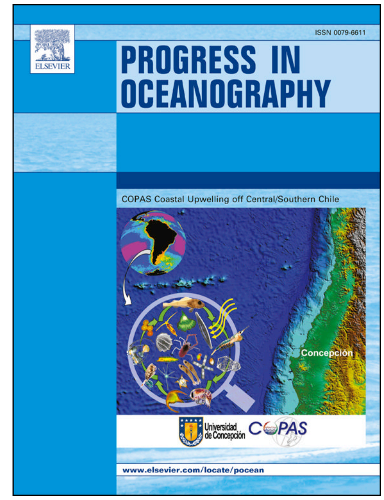

Two ‘faces’ of ENSO-induced surface waves during the tropical cyclone season

Yuchun Lin, Lie-Yauw Oey, Alejandro Orfila

PII: S0079-6611(18)30160-5
DOI: https://doi.org/10.1016/j.pocean.2019.03.004
Reference: PROOCE 2088

To appear in: *Progress in Oceanography*

Received Date: 17 May 2018
Revised Date: 28 February 2019
Accepted Date: 11 March 2019

Please cite this article as: Lin, Y., Oey, L-Y., Orfila, A., Two ‘faces’ of ENSO-induced surface waves during the tropical cyclone season, *Progress in Oceanography* (2019), doi: https://doi.org/10.1016/j.pocean.2019.03.004

Two 'faces' of ENSO-induced surface waves during the tropical cyclone season

Yuchun Lin[1], Lie-Yauw Oey[1*], and Alejandro Orfila[2]
1: National Central University, Taiwan
2: Instituto Mediterráneo de Estudios Avanzados, Spain
*Corresponding Author: lyooey@gmail.com

Abstract:

The response of the wave climate to tropical cyclones (TCs) is investigated using the significant wave height (SWH) observed from satellites and the WAVEWATCH III (WW3) model. Tropical cyclone wind generates local waves (wind seas) under the TC and longer-period waves (swells) that propagate long distances. The genesis location, intensity, and frequency of tropical cyclones over the global ocean are strongly affected by the phases of the El Niño Southern Oscillation (ENSO). It is shown that the interannual variation of global ocean surface waves in the subtropics during summer is dominated by ENSO-related TC activity. In particular, in the subtropical western North Pacific, the wind power is stronger in the TC season before an El Niño and weaker before a La Niña. These ENSO-related TC variations are shown, through composite and empirical orthogonal function analyses, as well as modeling, to dominate the spatial distribution and temporal variation of the SWH over the western North Pacific. The model confirms that longer-period waves (swells) are driven into northern South China Sea, toward Japan in mid latitudes and toward the central Pacific along the equator due to ENSO-related TC activities. The wind power and SWH over the subtropical western North Pacific lead and regress well with the ENSO index, suggesting that they may potentially serve as useful ENSO predictors.

1. Introduction

Ocean surface waves are important for upper-ocean mixing [Babanin, 2006]. Surface waves have been widely investigated using measurements taken from ships, buoys, satellites [Sandwell and Agreen, 1984; Gulev and Hasse, 1999; Young, 1999; Allan and Komar, 2000; Chen et al., 2002; Woolf et al., 2002; Gulev and Grigorieva, 2006; Thomas et al., 2008; Young et al., 2011] and model simulations [Kushnir et al., 1997; Sterl et al., 1998; Young, 1999; Cox and Swail, 2001; Vikebø et al., 2003; Stephens and Ramsay, 2014]. In general, at higher latitudes, surface waves have larger amplitudes in the winter hemisphere because of the correspondingly strong winds, while they are of smaller amplitudes in the summer hemisphere due to the correspondingly weaker winds [Sandwell and Agreen, 1984; Young, 1999]. Two types of wind-driven surface waves can be defined. One type of waves is called wind seas, which are waves dominated by local wind at the generation area and are generally of shorter periods and wavelengths. The other type is called swells, which are waves that have propagated away from their generation areas, or when the wave phase speed is greater than the wind speed [Semedo et al., 2011]. In general, swells travel long distances across ocean basins [Barber and Ursell, 1948; Munk et al., 1963; Snodgrass et al., 1966; Young, 1999; Chen et al., 2002] and account for about 75% of the waves observed over the global ocean [Semedo et al., 2011]. Swells are mainly generated from storms with high wind speeds at high latitudes [Young, 1999; Chen et al., 2002].

A tropical cyclone (TC) is a high wind-speed storm system in low to mid latitudes [Emanuel, 1991]. In the western North Pacific, tropical cyclones are also called typhoons, although strictly speaking they are TCs of Category 1 and above. On average, at least 5 typhoons per year make landfall on the coast of East Asia, and more TCs have tended to shift northward in recent decades [Oey and Chou, 2016]. Intense TC winds with speeds over 30 m s^{-1} and reaching 75 m s^{-1} or more generate high waves of more than 5 m over the open ocean [Young, 2003, 2006]. Tremendous waves and storm surges cause loss of lives and huge damage on properties and infrastructure along the affected coasts [Needham et al., 2015]. The effect is magnified when a storm surge encounters high tides [Tolman, 1991]. Taiwan, which is often along the path of TCs, is adversely affected by the heavy rainfall, flooding, and erosion induced by TCs [Yang et al., 2010; Huang and Wang, 2015; Chen et al., 2017]. In addition, strong TC wind produces upper-ocean mixing that can cause chlorophyll-a blooming in the oligotrophic western North Pacific [Lin and Oey, 2016].

Many studies have shown that TC-generated waves still satisfy the fetch- and duration-limited wave growth function, because the high wind speeds outrun the waves, which generally have slower speeds [Young, 1988, 1998, 2003, 2006; Young and Vinoth, 2013; Hwang, 2016; Hwang and Walsh, 2016]. In the northern, or southern, hemisphere, higher waves are mostly located on the right, or left, side of the TC where the most intense wind is. Observations of wave distributions inside TCs have shown that younger waves are located on the back side of the TC, and older waves with longer wave periods are on the front side [Hwang, 2016; Hwang and Walsh, 2016]. These previous studies mainly focused on waves under the influence of TCs. Waves that propagate from TCs are seldom discussed. For example, the climatology of wind seas of significant wave height (SWH) from July to September has a local high in the western North Pacific east of Taiwan and south of Japan (e.g., see Fig. 5c from Fan et al. [2014]), a region that is frequented by typhoons during the summer. The region of higher swell SWH, on the other hand, extends northeastward past Japan and reaches the Bering Sea (see Fig. 6c from Fan et al. [2014]). In this study, we will demonstrate that these patterns are produced by TCs.

The interannual TC activities in the western North Pacific are affected by the El

Niño Southern Oscillation (ENSO). Chia and Ropelewski [2002] suggested that ENSO changes the genesis locations of TCs by changing the vertical wind shear, the sea surface temperature, the monsoon trough, and the western Pacific subtropical high. Studies have shown that the intensity and frequency of TCs tend to be higher in the summer before a positive ENSO i.e. El Niño (i.e., developing El Niño summer) and lower in the summer before a negative ENSO i.e. La Niña [Harr and Elsberry, 1991, 1995; Chan, 1994; Lander, 1996; Chan, 2000; Camargo and Sobel, 2005]. Higher sea surface temperature in the central Pacific during a developing El Niño summer makes TCs more likely to form further east [Lander, 1994; Chan, 1985] and to curve northward [Elsner and Liu, 2003]. Although general wave climatology and waves driven by TCs are well established in previous studies, the wave climate under the influence of ENSO-related changes in TCs is rarely mentioned.

The behaviors of tropical cyclones in other global ocean basins are also affected by ENSO, either directly or through atmospheric teleconnections. Eastern North Pacific TCs are strongly affected by ENSO since the sea surface temperature (SST) anomaly in the central Pacific changes the surrounding environment [Chu and Wang, 1997; Collins, 2000; Camargo et al., 2008; Toma and Webster, 2010; Balaguru et al., 2013]. South Pacific TCs tend to form further east over the warm pool region during El Niño years and form further west closer to the east coast of Australia during La Niña years [Nicholls, 1984 and 1985; Solow and Nichols, 1990; Liu and Chan, 2012; Ramsay et al., 2012]. North Atlantic TC activities are out of phase with ENSO due to strengthening (weakening) of upper-level westerly and vertical wind shear in the summer before El Niño (La Niña) [Gray, 1984; Tang and Neelin, 2004; Shaman et al., 2009]. Both El Niño and a positive Indian Ocean Dipole (IOD) create unfavorable conditions for TC genesis in the eastern Indian Ocean [Xie et al., 2002; Lau and Nath, 2003; Ho et al., 2006; Ash and Matyas, 2012]. A warm SST anomaly in the Niño-3.4

region changes the Walker circulation along the tropical area and creates an anomalous anticyclonic circulation in the atmosphere that suppresses TC formation over the eastern South Indian Ocean [Ho et al., 2006; Kuleshov et al., 2008, 2009]. Strengthened trade wind upwells cold water in the eastern Indian Ocean, which would reduce TC formation during Positive IOD. The interaction of ENSO and IOD can significantly affect TC trajectories in the Southern Indian Ocean [Ash and Matyas, 2012].

Our goal is to understand the variations of ocean surface waves and their connection to ENSO-related tropical cyclone activity. We will demonstrate that ocean waves are closely linked to ENSO-induced changes in the frequency and intensity of TCs, as a *group*. Our work is not about the intensity change of an *individual* typhoon, which is a complex, yet unsolved scientific problem regardless of when the change occurs: strong or weak, El Nino or La Nina, since ENSO is inter-annual while time scales for individual typhoon intensification processes are hours ~ days [for a recent overview please see Zhang and Oey 2019a].

Section 2 describes the satellite data, the WAVEWATCH III model, and methods used in this study. Section 3 presents and discusses the results and the relationship between surface waves and ENSO-related tropical cyclone activity, first for the western North Pacific and then for the other global ocean basins. Conclusions are given in section 4.

2. Data and Methods

Satellite SWH:

We used global (80°S to 80°N) along-track satellite SWH data (ftp://ftp.ifremer.fr/ifremer/cersat/products/swath/altimeters/waves/) for the time period from Jan 1, 1993 to Dec 31, 2016. The data combine measurements from 9 altimeters, namely, ERS-1&2, TOPEX-Poseidon, GEOSAT Follow-ON (GFO), Jason-1, Jason-2, ENVISAT, Cryosat, and SARAL. Details on the data and how they are processed are given at the Ifremer link above. The along-track resolution is approximately 7 km and the temporal resolution is approximately 1 second. Previous studies used altimeter-measured SWH for the global ocean and regional seas by monthly averaging the along-track SWH onto 2°×2° grid cells to ensure sufficient data coverage [Young, 1999; Woolf et al., 2002; Young et al., 2011]. Woolf et al. [2002] mentioned that a single satellite is usually sufficient to reach the sampling condition of Cotton and Carter [1994]. Here we monthly averaged the along-track SWH onto 1°×1° grid cells and used a two-dimensional Gaussian filter to fill the grid cells with missing data in order to smooth the data. On average, the missing data are about 1.2% of the total data.

The number of satellite data varies with time and generally increases over time (Supplementary Material Fig.S1). To make sure that our analyses are unaffected by the varying sampling number, we check first if the different numbers of sampling in early and later satellite periods may degrade our analysis data. We compare the satellite SWH against the SWH measured at 57 buoys from the National Data Buoy Center (NDBC) in the Pacific and Atlantic Oceans. We check for the entire 1993-2016 period, and two shorter periods from 1993 to 2000 and also from 2009 to 2016. The global averaged track densities are ~70 and ~110 per $1^o\times1^o$ grid in the earlier and later periods, respectively. The comparison is shown as regressions for the three periods in Supplementary Material Fig.S2. The regression slopes/R^2 for the three periods (1993-2016, 1993-2000, 2009-2016): (0.847/0.774, 0.819/0.761, 0.854/0.769), are close to each other, suggesting insensitivity to the different number of sampling in the different periods. We next check the sensitivity of our ENSO composites (below) by repeating the analyses for two separate, shorter periods: 1993-2004 and 2005-2016, as well as the complete 1993-2016 periods. The results are similar (Supplementary Material Fig.S3).

Wind data:

We used the data-assimilated reanalysis wind from the Cross-Calibrated Multi-Platform version 2 (hereafter CCMPV2) [Atlas et al., 2009; Wentz et al., 2016] data to help interpret and understand the surface wave climate. CCMPV2 wind has a 1/4°×1/4° spatial resolution and a 6-hour temporal resolution covering from 78.375°S to 78.375°N and from July 1987 to present. CCMPV2 wind underestimates the strong winds associated with TCs [Sun and Oey 2015; Sun et al., 2015; Oey and Chou, 2016; Liang et al. 2017; Zhang and Oey 2019a,b]. Therefore, a parametric TC wind vortex model with parameters averaged from different TC centers from the Interannual Best Track Archive for Climate Stewardship (IBTrACS) data set [Knapp et al., 2010] is used to correct the CCMPV2 wind [Oey and Chou, 2016], as described more recently in details by Zhang and Oey [2019a,b]. Thus the 10-m wind near the TC is first calculated using a parametric tropical cyclone model [Holland et al., 2010] using 6-hour center pressure, location, and V_{max} from the IBTrACS set, with the radius of maximum wind estimated from Knaff et al. [2007] and the cyclone moving component added following Jakobsen and Madsen [2004]. The tropical cyclone wind is then merged with the CCMPV2 reanalysis wind at a radial distance where their differenced wind speed is least, which is generally >~350 km from the cyclone center. Supplementary Material Fig.S4 shows an example of the resulting wind field for Typhoon Haiyan (2013). Six-hour wind stress is calculated using the wind-drag formula from Oey et al. [2006; 2007], which has a high wind-speed drag coefficient (C_d) limit as in Powell et al. [2003].

Another TC-only wind field is generated using the Holland vortex model alone without the CCMPV2 environmental wind to isolate the effects of TC on surface waves. The two wind fields are used to drive the WAVEWATCH III model, as will be discussed later.

The 6-hour IBTrACS dataset is also used to calculate the number of TCs, the TC visitation frequency, and the accumulated cyclone energy (ACE) from June to November (December to May of the following year) of each TC season in the northern (southern) hemisphere. Only TCs with maximum sustained wind greater than 33 m s^{-1} (Category 1) are considered. The TC visitation frequency is calculated by counting the number of TCs in 5°×5° grid cells for each year [Sun and Oey 2015; Oey and Chao 2016; Liang et al. 2017]. The ACE formula is calculated by summing the squares of the TC maximum sustained wind (divided by 10^4) through each TC lifetime [Oey and Chao 2016]. In the western North Pacific, the ACE has been found to be related to the following ENSO for up to six months [Camargo and Sobel, 2005]. The ACE is used here to assess the TC intensity for each year.

<u>Wave model</u>:

A wave hindcast was conducted using WAVE WATCH III™ version 5.16 (WW3) [WW3 Development Group, 2016] to analyze the effects of ENSO on the SWH in the Pacific Ocean. In particular, the modeled wave peak period and directions will be used to supplement the satellite observations. Model SWH is used to validate the WW3 performances by comparing with observed SWH and study the responses of surface height. Peak wave period can be used to calculate the dimensionless parameter ω_n, which is the inverse of wave age, for determining the wind sea and swell. Wave directions are for indicating the wave propagations. The WW3 integration is from January 1992 to December 2016, which includes a one-year spin-up run at the beginning. The domain covers the Pacific Ocean from 98.5°E to 66.8°W and 66°S to 69.3°N. The resolution is $1/3^{o}\times1/3^{o}$, 35 frequencies (f) from 0.041 Hz to 1.05 Hz and 36 directions of equal 10^{o} interval [see http://mpipom.ihs.ncu.edu.tw/showForecasts/Waveperiod.php]. Tolman and Chalikov's [1996] source terms are used, and the input 10-m wind (U10) is modified using the 'effective' wind formulation of Tolman [2002] to account for the instability of the atmospheric boundary layer. We assume an f^{-5} spectral tail outside the model frequency range, as used in the default WW3 settings. The default third order advection scheme is used for spatial propagation of the wave spectrum. Other details can be found in Tamura et al. [2012]. The WW3 output is daily at 00:00UTC. The model focuses in the Pacific to examine the largest responses of ENSO-related TC wave in the western North Pacific. The effects of inter-basins and lateral boundaries are relative small since the connections to other basins are in the Southern Ocean. Two WW3 experiments driven by two different winds were conducted: one is the merged Holland vortex and the CCMPV2 wind field and the other is Holland vortex wind only. The daily WW3 output is also monthly averaged for the composite and empirical orthogonal function analyses, similar to the method applied to the observed data.

Model validations:

In Tamura et al. [2012], the performance of the WW3 modeled Stokes drift was validated against the estimated Stokes drift based on observed frequency spectra at NDBC buoys in the Pacific; the agreements were generally good. For the present study focusing on the SWHs, we validate the model SWHs (Supplementary Material Fig.S5c) against those obtained from the North Pacific Ocean buoys from the National Oceanic and Atmospheric Administration (NOAA)/National Data Buoy Center (NDBC), for the period from Jan 1993 to Dec 2016 (Supplementary Material Fig.S5a); for comparison, we repeated the same validation for the satellite SWHs as well (Supplementary Material Fig.S5b). The buoys are located off the western coast of USA and around the islands of Hawaii and Guam. The SWH's being compared include both wind seas and swells. The regressions of satellite and WW3 SWH with buoys at the grid points closest to the buoys show good agreements between buoys and satellite, and between buoys and WW3 SWHs. The agreements between model and buoy are excellent, with an R^2 of 0.92, near-unity slope of 0.88 and nearly zero bias, all significant at the 99.99% confidence level. The satellite-buoy comparison is also good: R^2 = 0.7 and slope = 0.74.

The above comparison with buoy data include both TC-induced and non-TC-induced waves, including swells. We now validate the modeled SWHs directly under the TCs against the SWHs obtained from the satellite data. To do this, we note that under strong TC winds, excluding the region near the eye, the inverse wave age is generally greater than 1; this was previously shown from *in situ* [Hwang and Walsh 2016] and satellite observations [Zhang and Oey 2019b]. Hwang and Walsh [2016] show that the corresponding dimensionless wave growth functions are then comparable to those in field experiments collected under more ideal quasi-steady fetch-limited conditions [Toba 1972; Donelan et al. 1992; Hwang and Wang 2004; Mellor et al. 2008]. We therefore calculate various wave parameters using the Hwang and Walsh's wave-growth functions and compare them with the WW3 model outputs. The comparison for the peak wavelength is shown in Supplementary Material Fig.S6; comparisons of other parameters such as the peak periods and phase speeds yield similar results as they are constrained to satisfy the dispersion relation. The plot indicates that the WW3 model does reasonably well in simulating the dominant TC-induced wind seas directly under the TCs (near-perfect regression (red) line with highest data density in the 70 m ~< λ_p <~ 300 m range). The plot shows that the WW3 also simulates swells [e.g. Moon et al. 2003; Holthuijsen et al. 2012] with wavelengths longer than can be approximated by formulae based on the wave-growth functions.

ENSO composites:

The ENSO index characterized by the SST anomaly in the Niño-3.4 region (5°S-5°N, 120-70°W) is used [Barnston et al., 1997]; the data were obtained from the National Center for Atmospheric research (NCEP) Climate Prediction Center. The IOD index is defined as the SST anomaly between the western Indian Ocean (10°S-10°N, 50-70°E) and the southern east equatorial Indian Ocean (10°S-0°N, 90-110°E) [Saji et al., 1999]; the data were obtained from National Oceanic and Atmospheric Administration (NOAA)/Earth System Research Laboratory (ESRL). Figure 1 shows the ENSO and IOD indices during our study period. The IOD index is mostly positive and tends to be larger during El Niños (e.g. 1994/1995 and 1997/1998). El Niño usually develops from a normal year and switches to La Niña in the following year. On the other hand, La Niña can continue for several years from a previous year's well-developed La Niña. The ocean status could remain from previous La Niña and thus the upper ocean responses to the second La Niña could be enhanced. This study focuses on the spatial distribution and temporal variation of the SWH, wind field, and WW3 model outputs during the El Niño and La Niña TC seasons. The ENSO composites of a variable such as the SWH were therefore calculated as averages for June-November months when the ENSO index was greater than +1 for the El Niño composite and when the index is less than -1 for the La Niña composite. During the study period, there were seven such positive ENSO events—1994, 1997, 2002, 2004, 2006, 2009, and 2015—and seven negative ENSO events—1998, 1999, 2005, 2007, 2008, 2010, and 2011.

We will show the differences between El Niño and La Niña (the former minus the latter) using composites. The significance of the difference is calculated at a 95% confidence level using the two-sided Wilcoxon rank sum test [Wilcoxon, 1945; Huang and Oey 2018].

3. Results

Figure 2 shows the composites from 1993 to 2016 of the SWH, wind power and wind speed anomalies, which subtracts the total mean, during the most active tropical cyclone season from August to October. The results are similar for other summer months except that the composite magnitudes are weaker. Wind power (Watts m^{-2}) is estimated as $\rho_a C_d V^3$, where ρ_a = 1.23 kg m^{-3} is the air density, C_d is the drag coefficient with a high wind-speed limit [Oey et al., 2006; 2007], and V is the 10-m wind speed in m s^{-1}. To quantify the degree of similarity between the SWH pattern and the wind power or wind speed patterns, we add dots in Fig. 2b,c to indicate where more than 80% of the wind power or speed within 5°×5° squares are of the same sign as the sign of SWH. It is clear that the pattern of the SWH (Fig. 2a) in the western North Pacific is more similar to the wind power (Fig. 2b) than the wind speed (Fig. 2c). The reason is because wind power more directly characterizes the rate of wind energy input into the ocean to generate waves. The rate of change of the total, frequency-integrated, wave energy is in fact proportional to the cubed of the wind speed (minus dissipation), and the significant wave height in turn may be related to the wave energy [e.g. Hwang and Sletten 2008; Mellor et al. 2008; Donelan et al. 2012; Hwang and Walsh, 2016]. Now, taking the cubic power of the wind speed accentuates stronger winds. The similarity of the SWH and wind power patterns in Fig. 2a,b therefore suggests that waves in the western North Pacific in summer may be mostly caused by passages of tropical cyclones.

Figure 3 shows the composite maps of TC frequency and wind power for El Niño (Fig.3a,c) and La Niña (Fig.3b,d). The TC frequency is generally higher and more widespread during El Niños than during La Niñas; the higher frequency during El Niños is contributed by longer traverse distances covered by the TCs as their genesis locations shift eastward. The wind power (Fig.3c,d) also show similarly higher and more widespread composites for El Niños than La Niñas, confirming that higher wind power is mostly contributed by TCs. East of the Philippines and Taiwan, the TC frequency contour of 12 hours month^{-1} encompasses the region of higher wind power > 1 Watt m^{-2}. There is also a moderately high wind power region east of Japan, contributed in part by the strong mid-latitude westerly and extra-tropical cyclones that begin to appear in October and November in that region [Nakamura et al. 2004].

Figure 4 shows the composite differences (El Niño *minus* La Niña) of the TC frequency, wind power and significant wave height. Positive differences of the wind power and the TC visitation frequency [e.g. Oey and Chou 2016] indicate that TCs are stronger and longer lasting during El Niño than during La Niña. The difference in the TC visitation frequency between El Niño and La Niña TC seasons is significantly positive at a 95% confidence level over the tropical-subtropical western North Pacific east of 130°E and from 10° to 25°N (Fig. 4a). The positive difference is due to the number of yearly TCs being slightly more for El Niño, 14±2, compared to 11.4±3.3 for La Niña, and also because during El Niño TC genesis points are generally more to the east nearer the dateline and TCs cover longer distances and have longer lifetimes, as mentioned above. There is slightly less (more) TC activity in the SCS during El Niño (La Niña) [Sun et al. 2017], but the difference is insignificant. The maximum TC visitation frequency is 20 hours per month during El Niño and 16 hours per month during La Niña (Fig.3a,b). The largest difference in the TC visitation frequency is 9 hours per month with two highs over the western North Pacific.

Figure 4 also shows that the positive differences in SWH and wind power are collocated with the positive difference in the TC visitation frequency. The largest positive SWH difference (Fig. 4c) is closely collocated with the strongest wind power difference (Fig. 4b) east of Taiwan and Luzon from 15° to 25°N and between the 130° to 150°E longitudes. The wind power difference decreases more abruptly north and south of this sub-region, but the region of significantly positive SWH difference decreases more gradually and covers a wider area than the wind power and TC visitation frequency. In the South China Sea, a north–south dipole structure appears in the SWH and wind power, but not in the TC visitation frequency; the latter instead shows generally less (more) TCs during El Niño (La Niña). The southern positive part of the wind power and SWH dipole is therefore not related to TCs, but rather is caused by the stronger southwesterly monsoon wind during El Niño compared to La Niña [e.g. Oey et al 2013]. On the other hand, the northern negative part of the dipole, while insignificant, may be due to decreased (increased) TC activity during El Niño (La Niña), mentioned above. However, Figs.4b & 4c show that the monsoon-induced wind power and SWH variability in South China Sea are much weaker (and insignificant for SWH) than the dominant TC-induced variability.

The collocated areas of high wind power and SWH (Figs. 4b,c) suggest that waves in those areas may contain more wind seas than swells, generated by the more frequent passage of longer-lasting and stronger TCs during El Niño. On the other hand, south of Japan, away from the high wind power region, the waves may be mostly swells that have traversed from the high wind power area in the southwest.

To demonstrate that it is the wind power rather than wind speed that controls the yearly variation of the significant wave height, we plot the time series of wind power and speed (Fig.5a), as well as the observed SWH (Fig.5b blue line) averaged from June through November and within the area from 120°E–180°E, and 5°N–40°N; the ENSO index is also plotted (red). The SWH can be seen to co-vary well with the wind power, but less so with the wind speed. The correlations (r) between the observed SWH and wind power, and between the SWH and wind speed are 0.89 and 0.59 (both 99.9% confidence), respectively. The wind power is also better correlated with ENSO, with r = 0.75 (99.9% confidence) compared to r = 0.34 (90% confidence) for the correlation between the wind speed and ENSO. These results indicate that wind power rather than wind speed is the factor that controls the SWH.

The similar interannual variations of the SWHs, wind power and ENSO suggest, since the peaks of wind power and SWH precede the ENSO peak, that SWH and wind power over the western North Pacific *subtropical* ocean may potentially serve as useful predictors of the ENSO intensity. To explore this, we regress ENSO (averaged from December through the following year's February), the predictand, against the SWH and wind power, the predictors, averaged over the dashed rectangle shown in Fig.4b, and from June through November (Fig.6a,b; i.e. 3~6 months in advance of the peak ENSO). The averaging rectangle is chosen where the composite differences (El Niño *minus* La Niña) of TC frequency, wind power and SWH are highest (Fig.4). For moderate and higher-intensity ENSO events, i.e. $|\mathrm{ENSO}| \geq 0.5$ (blue lines), the (r^2, s) = (0.66, 0.96) for the SWH and (0.62, 0.92) for the wind power, where s is the slope of the regression line. For strong ENSO events, i.e. $|\mathrm{ENSO}| \geq 1$ (red lines), the (r^2, s) = (0.88, 1.33) for the SWH and (0.94, 1.35) for the wind power. It is notable that, for both cases, the corresponding slopes are nearly equal, consistent with the above inference that SWH and wind power are closely related. As a measure the goodness of these predictors, we compare the above r^2 against those obtained from the regression of the wind speed averaged over the west-central equatorial Pacific within the rectangle indicated in Fig.6d (within the Niño-4 region https://www.ncdc.noaa.gov/teleconnections/enso/indicators/sst.php), chosen to encompass the region where the dominant Empirical orthogonal function (EOF; see below) for wind speed is highest (Fig.6d). Here, the equatorial trade wind weakens (strengthens) during an El Niño (a La Niña). The corresponding wind speed averaged from June through November is a good predictor of ENSO (Fig.6c), with (r^2, s) = (0.81, -1.09) for $|\mathrm{ENSO}| \geq 0.5$, and (r^2, s) = (0.86, -1.24) for $|\mathrm{ENSO}| \geq 1$. The r^2 values are comparable to those relating ENSO to SWH and wind power (Fig.6a,b).

Empirical Orthogonal Function (EOF):

Empirical orthogonal function is a powerful tool for identifying patterns of variability [Kutzbach 1967]. While EOF modes are not dynamical modes, they can provide, when interpreted with some physical foresights, useful information on dynamical processes [Kundu et al. 1975; Oey et al. 2004, 2009; Lin XH et al. 2007; Oey 2008; Xu and Oey 2011, 2015; Chang and Oey 2012; Wang and Oey 2014, 2016; Lin YC et al. 2016; Huang and Oey 2018]. An EOF analysis is applied to the SWH and wind to describe the dominant spatial characteristics of TC-induced waves. Figures 7 show the first EOF modes of the SWH (Fig. 7a), wind power (Fig. 7b), and wind speed (Fig. 5c). These mode-1s are well-separated from their respective higher modes according to the North et al's [1982] estimates for EOF degeneracy [e.g. Oey 2008]. The first mode of SWH contributes to 39% of the total variance. The eigenvector shows that the highest anomaly is east of Luzon. The contours spread northeastward toward Japan. The first principle component (PC1) of the SWH (Fig.7a) shows interannual variations and is significantly correlated with the ENSO index: Corr($PC1_{SWH}$, ENSO, 4 months) = 0.59. Here, Corr(A, B, lag) denotes the maximum lag correlation coefficient satisfying a 95% confidence level between the A and B with lags in months, which is positive if A leads B and negative otherwise [cf Chang and Oey 2012]. As ENSO peaks in December, the 4-month lead confirms that the dominant SWH fluctuation occurs during the TC season in summer and fall. The first mode of the wind power accounts for 17% of the total variance, and the $PC1_{Power}$ again leads ENSO by 4 months: Corr($PC1_{Power}$, ENSO, 4 months) = 0.58 (Fig. 7b). Its eigenvector has its largest amplitude east of Luzon, slightly to the west of the largest amplitude of the mode-1 SWH eigenvector (Fig. 7a). These 4-month leads on ENSO for $PC1_{SWH}$ and $PC1_{Power}$ (as well as $PC1_{Speed}$ below) and their eigenvector patterns indicate the existence of TC-induced SWH and wind in the summer/fall *prior* to the peak ENSO. The next dominant mode-2's are weaker than and well-separated from mode-1's, and moreover they all *lag* ENSO (Supplementary Material Table S1). In the case of SWH, Fig.7a indicates that waves spread after being generated by TCs. As there are more re-curving TCs than westward TCs [Elsner and Liu, 2003], the spreading is predominantly north-northeastward toward Japan. During the summer before an El Niño, the spreading of positive anomaly indicates that more waves reach southern Japan, produced by the increased number of re-curving TCs, and *vice versa* during a La Niña. On the other hand, in the case of the wind power, the largest variability is localized east of Luzon between about 130^{o}E to 135^{o}E longitudes, near where the TC frequency is highest (Fig. 3a,b).

The first mode of the wind speed (Fig. 7c) accounts for 20% of the total variance, and the PC1$_{Speed}$ leads ENSO by 4 months: Corr(PC1$_{Speed}$, ENSO, 4 months) = 0.46. The wind speed eigenvector shows also the maximum east of Luzon similar to that for the mode-1 eigenvector of the wind power, but the area of large wind speed eigenvector spreads more eastward. A secondary maximum is also found in the southern portion of the South China Sea, caused by the interannual variation of the southwesterly monsoon wind mentioned above (i.e. Fig. 4). Thus in the summer and fall prior to the peak of an El Niño (a La Niña), the southwesterly monsoon wind generally strengthens (weakens). This wind speed pattern in the South China Sea would explain the dipolar differenced pattern (i.e. El Niño – La Niña) of Fig. 4c for the significant wave height. The mode-1 EOF signal in the South China Sea is weak however, since the EOF pattern is dominated by the strong signal due to waves generated by TCs in the open western Pacific east of Luzon (Fig. 7a).

<u>The WW3 Model Results</u>:

To gain a better understanding of the characteristics of TC-induced waves, we now examine the SWH, peak wave period, and wave directions obtained from the WW3 model. The model was driven by two different types of wind fields. One was the merged CCMP and Holland vortex model wind (hereinafter referred to as the 'merged wind') and the other was the Holland vortex model wind only (hereinafter 'Holland wind'; see Methods). The first type of wind field produces both TC-induced waves and waves due to the large-scale wind field such as the trade wind and/or other weather events such as, for examples the southwesterly monsoon wind bursts and the Madden-Julian oscillation (MJO) [Madden and Julian, 1971, 1972]. The second type of wind field produced TC-induced waves only. We first validate the model by comparing the model results forced by the merged wind with the observation. We then discuss the wave distributions forced by the two types of wind.

Figure 8a shows the difference between the El Niño and La Niña composites for the model SWH. It agrees well with the observed SWH composite difference (Fig. 4c), although the model SWH shows a larger difference. The larger model difference extends further north and to the east of Japan. Figure 5b compares the yearly variations of the observed and model SWHs averaged from June through November and within the area from 120°E–180°E, and 5°N–40°N. The model SWH nearly reproduces the variation and amplitude of the observed SWH, with r = 0.91 (99.9% confidence). The observed SWH has a slightly higher correlation with the ENSO than the model SWH: r = 0.77 for the observed SWH and r = 0.73 for the model SWH, both leading ENSO by 3 months at the 99.9% confidence level.

We repeated the EOF analysis on the model SWH, both for the case forced by the merged wind (Fig. 8b) and for the case driven by the Holland wind (Fig. 8c). The first modes contribute to 41% and 76% of the total variances for the merged wind and Holland wind respectively. Both modeled eigenvectors show an almost identical distribution to the observed mode-1 SWH (Fig.7a) over the open basin. Thus the highest anomaly is located to the east of Luzon and the contours spread northeastward toward Japan. However, the mode-1 pattern for the merged wind case (Fig.8b) is more similar to the observed pattern, the % contribution to the total variances are both approximately 40%, and both of their principal component time series (PC1) agree very well (r = 0.83). Both patterns spread eastward in middle latitudes east of Japan under the influence of the westerly jet; they also show weak but discernible amplitudes in the South China Sea, forced by the southwesterly monsoon wind bursts mentioned previously. These mid-latitude and South China Sea signals are absent for the mode-1 SWH pattern for the Holland wind experiment (Fig.8c). Instead, the largest SWH is more concentrated east of Luzon and waves penetrate into the northern South China Sea and southern East China Sea through the gaps south and north of Taiwan.

The first principle component PC1 of the model SWH(*merged*) shows interannual variations and is significantly correlated with the ENSO index: Corr($PC1_{SWH\text{-}merged}$, ENSO, 3 months) = 0.59, very close to the observed correlation although the lead is 1 month shorter i.e. 3 months for model *vs.* 4 months for observation (Fig.7a). In contrast, the PC1 of SWH(*Holland*) shows an even higher correlation to the ENSO index: Corr($PC1_{SWH\text{-}Holland}$, ENSO, 3 months) = 0.81. Since ENSO (El Nino or La Nina) peaks in December, the 3-month lead of the modeled PC1 on ENSO indicates that the dominant modeled peak (maximum or minimum) tends to occur 3 months earlier in September, which is the month when the total number of re-curving (i.e. northward) TCs is largest (Fig. 9, red bars). Since the modeled lead is one month shorter than the observed lead, the model appears to be slightly biased in simulating larger waves produced by tropical cyclones, rather than smaller waves due to background, larger-scale wind fields.

The WW3 model provides information on wave periods and directions. Figure

10 shows the composite difference between El Niño and La Niña TC seasons for WW3 peak wave period. The peak wave period is significantly higher for El Niño TC seasons than for La Niña over most of the western North Pacific, except for the small region in southwestern South China Sea where the difference is negative but weak. The negative difference is produced because of stronger southwesterly summer monsoons in the developing phase of El Niño [Wang et al., 2008], which generate local wind seas with short periods. The largest (positive) difference is located east of Japan, indicating that waves generated by TCs during El Niño propagate farther over the open ocean, and therefore generally have longer periods.

We use the dimensionless parameter $\omega_n = 2\pi U_{10}/(gT_p)$, where T_p is the peak wave period in seconds calculated from WW3, U_{10} is the wind speed at 10-m elevation in m s^{-1}, and g is the gravitational acceleration in m s^{-2}, as the inversed wave age, such that younger (older) waves have larger (smaller) ω_n [Hwang et al., 2011]. Figure 11 shows the composite differences between the El Niño and La Niña TC seasons of the modeled SWH, peak wave period, ω_n, and wave vector. The left (right) column is for the model forced by the merged (Holland) wind. For the merged wind case (Fig. 11a-c), the difference between waves in El Niño and La Niña is predominantly to the east of ~135°E, and waves spread from the center where the observed wind power and SWH differences are largest (Fig. 4b,c). Thus waves spread more eastward and northward due to the predominance of TCs in the open ocean in El Niño compared to La Niña years. The differenced waves also spread more eastward near the tropics, partly driven by the TCs, but also by the stronger westerly wind bursts blowing from the South China Sea to the equatorial Pacific during El Niño compared to La Niña. Both the wave period and ω_n plots (Fig. 11b,c) confirm that waves reaching Japan are older with longer periods during El Niño compared to La Niña, while the eastward waves near the equator are younger. As the TCs are more energetic and of re-curving type during El Niño, the cyclonic TC wind steers waves toward Japan for the right-hand side and along the equator for the left-hand side. Larger waves are generated to the right and in front, respectively, of TCs by the relatively stronger TC winds in these two areas [Hwang, 2016; Hwang and Walsh, 2016; Zhang and Oey 2019b], and they radiate 'down path' as swells or older waves. Westerly wind bursts during the developing phase of El Niño also contribute to the weakening of the trade winds and generates Kelvin waves propagating eastward along the equator [Chen et al., 2016]. These waves therefore have relatively long periods and are older in the central Pacific during the developing phase of El Niño.

For the Holland wind case (Fig. 11d-f), the differenced SWH radiates outward to the north and west from where the observed TC frequency, wind power and SWH differences are largest (Fig. 4). The eastward waves in the tropics, found for the merged wind experiment (e.g. see vectors in Fig. 11a) are generally absent, confirming the importance of the non-TC, southwesterly/westerly wind bursts to the generation of younger waves near the coast of Indonesia and Philippines, but older, longer-period waves along the equator further east. However, comparing Fig. 11f with Fig. 11c, we see that waves induced by TCs during their early stages near the genesis locations (see Fig. 4a) also produce swells along the equator. The waves are also generally older with longer periods over the entire western North Pacific basin, especially along the coast of East Asian continent from South China Sea to Japan. These swells propagate from the open Pacific, produced by the TCs. Comparing the Holland wind and merged wind experiments, it is clear that the background, non-TC winds, including the southwesterly monsoon winds, are important in generating younger and shorter-period waves that influence almost all the marginal seas of East Asia.

<u>ENSO effects on global TC-induced waves</u>:

While our focus is primarily on waves during the TC seasons in the western North Pacific, it is interesting to also examine the differences between El Niño and La Niña TC seasons of the observed SWH, wind power, and TC visitation frequency in the other basins of the global ocean. In the southern hemisphere, we define the TC season to be from December to May of the following year. Figure 12 shows that significant positive differences in the TC visitation frequency composites are located in the western and central North Pacific, the central South Pacific, and the central South Indian Ocean. Significant negative differences are mainly located in the North Atlantic and the eastern South Indian Ocean. The differences in the SWH and wind power composites are collocated well with the changes in the TC visitation frequency composites. Thus areas of higher (lower) SWH and wind power differences with the red (blue) color shadings are generally collated with higher (lower) TC frequency differences with white (black) contours. In El Niño years in the eastern North Pacific, warmer SST anomalies reduce the vertical wind shear and tend to favor TC activity [Landsea, 2000]. However, strengthened Central American Gap winds generate unfavorable conditions for TC genesis near the Mexico coast region [Fu et al., 2017]. These subtle differences in the TC activity result in west-to-east SWH and wind power contrasts in the eastern tropical North Pacific, from ~160^{o}W to ~80^{o}W. In the south Pacific, the warmer SST remains to the east after the peak of El Niño; more TCs then tend to form near the Date Line, and less TCs off eastern Australia [Nicholls, 1984, 1985; Solow and Nichols, 1990; Ramsay et al., 2012]. The SWH and wind power, therefore, are significantly higher to the east and lower to the southwest close to the east of Australia. The activities of North Atlantic TCs, in relation to the ENSO, are out of phase with the western North Pacific TCs. The warmer SST anomaly in the eastern Pacific increases the vertical wind shear over the tropical region of the North Atlantic during El Niño [Shaman et al., 2009]. This vertical wind shear suppresses the formation of TCs over the Caribbean Sea, reduces the wind power, and lowers the SWH composites in the North Atlantic. In the South Indian Ocean, the east-west TC visitation frequency contrast is strongly influenced by both ENSO and IOD. During the peak of El Niño, an anomalous anticyclonic circulation on top of the eastern South Indian Ocean is formed due to the warmer SST in the eastern Pacific, which suppresses the formation of TCs [Ho et al., 2006]. A positive IOD is associated with cooler SST in the southeast Indian Ocean and warmer SST in the southwest Indian Ocean [Saji et al., 1999], causing TCs to form near the central Indian Ocean [Ash and Matyas, 2012]. In this study period, IOD is mostly positive and larger positive IODs are generally followed by El Niño (Fig. 1). The TC visitation frequency is therefore significantly reduced in the eastern portion of the South Indian Ocean during El Niño compared to La Niña, and the TC frequency is slightly more though insignificant in the central basin. The differenced SWH and wind power display similar east-west contrasting patterns that correspond to the TC visitation frequency. Significant changes in the SWH and wind power are mainly located in the eastern South Indian Ocean.

4. Conclusions

In this study, we analyzed observed significant wave heights (SWHs) from satellite and conducted model simulations of ocean surface waves to demonstrate that the interannual variation of global ocean surface waves in the subtropics during summer is dominated by ENSO-related tropical cyclone (TC) activity. The main focus was on the Pacific Ocean but the ENSO influence on other ocean basins was found to be also significant. Our findings are:

1. The eastward shift of warmer SST anomaly in the equatorial Pacific Ocean during the summer before an El Niño results in stronger and longer-lasting TCs, and *vice versa* during the summer before a La Niña when the warmer

SST shifts west. The contrast in TC paths and intensity between El Niño and La Niña results in higher wind power and SWHs over the western and eastern North Pacific;

2. The summer wind power and SWH over the subtropical western North Pacific correlate well with 4~6 month lead on the peak ENSO index from December to February of the following year. The regression is comparable to, and for strong ENSO events (|Niño 3.4| > 1) even higher than, the regression of ENSO with wind speed changes over the equator, suggesting that the wind power and SWH may serve as additional useful ENSO predictors;
3. In subtropical western North Pacific, largest wind power and SWHs are located east of Luzon near 135^{o}~140^{o}E, coinciding with the region of highest frequency of TC passages. EOF analysis of the observed SWHs and the model results with and without the large-scale (i.e. non-TC) wind indicate that more swells spread northeastward toward Japan before El Niño than La Niña, produced by the corresponding increase in the frequency of re-curving TCs;
4. On the other hand, in the western tropical Pacific east of Indonesia, and in the southern South China Sea, waves are dominated by younger wind seas during an El Niño compared to a La Niña, caused by increased (decreased) westerly and southwesterly monsoon winds over the region in the summer before the peak El Niño (La Niña);
5. The model simulations with and without the large-scale (i.e. non-TC) winds confirm that energetic TCs prior to a peak El Niño generate waves with longer periods, which then travel long distances as swells. Wave directions from the models confirm that waves are then mainly steered toward Japan by the increased number of re-curving TCs. Moreover, these longer-period

waves also leak through the Luzon Strait into the northern South China Sea;

6. Through atmospheric teleconnection, the ENSO affects TC activities in other global ocean basins, as have been noted in previous studies. The resulting contrast in TC paths and intensity between El Niño and La Niña causes higher (lower) wind power and SWHs over the central South Pacific and western South Indian Oceans (North Atlantic and eastern South Indian Oceans).

Acknowledgements

We thank six anonymous reviewers for their comments, which improved the manuscript. Authors were supported by Taiwan Ministry of Science & Technology Grant#106-2611-M-008-001, awarded to the National Central University. Authors' contributions: LYO conceived and designed the study. YCL and LYO wrote the paper, with contributions from AO. YCL analyzed the data and plotted the figures. LYO interpreted the results with significant contributions from YCL and AO. All authors discussed the results.

References

Allan, J. and Komar, P., 2000: Are ocean wave heights increasing in the eastern North Pacific?. *Eos, Transactions American Geophysical Union 81*: doi: 10.1029/EO081i047p00561-01. issn: 0096–3941.

Ash, K. D., and C. J. Matyas, 2012: The influences of ENSO and the subtropical Indian Ocean dipole on tropical trajectories in the southwestern Indian Ocean, *Int. J. Climatol.*, 32, 41–56.

Atlas R., Hoffman R. N., Ardizzone J., Leidner S. M., Jusem J. C., 2009: Development of a new cross-calibrated, multi-platform (CCMP) ocean surface wind product. AMS 13thConference on Integrated Observing and Assimilation Systems for Atmosphere, Oceans, and Land Surface (IOAS-AOLS).

Babanin, A. V., 2006: On a wave-induced turbulence and a wave-mixed upper ocean layer, *Geophys. Res. Lett.*, **33**, L20605, doi:10.1029/2006GL027308.

Balaguru, K., Leung, R. L. and Yoon, J.-H., 2013: Oceanic control of northeast Pacific hurricane activity at interannual timescales. *Environ. Res. Lett.*, **8**, 044009.

Barber, N. F., and F. Ursell, 1948: The generation and propagation of ocean waves and swell. I. Wave periods and velocities. *Philos. Trans. Roy. Soc. London*, A240, 527–560.

Barnston, A.G., M. Chelliah and S.B. Goldenberg, 1997: Documentation of a highly ENSO-related SST region in the equatorial Pacific. *Atmosphere-Ocean*, **35**, 367-383.

Camargo, S. J., and A. H. Sobel, 2005: Western North Pacific tropical cyclone intensity and ENSO. *J. Climate*, **18**, 2996–3006.

Camargo, S. J., A. W. Robertson, A. G. Barnston, and M. Ghil, 2008: Clustering of eastern North Pacific tropical cyclone tracks: ENSO and MJO effects. *Geochem. Geophys. Geosyst.*, **9**, Q06V05. doi:10.1029/2007GC001861.

Chan, J. C. L., 1985: Tropical cyclone activity in the northwest Pacific in relation to El Niño/Southern Oscillation phenomenon. *Mon. Wea. Rev.*, **113**, 599–606.

Chan, J. C., 1994: Prediction of the interannual variations of tropical cyclone movement over regions of the western North Pacific. *Int. J. Climatol*. **14**, 527–538.

Chan, J. C. L., 2000: Tropical cyclone activity over the western North Pacific associated with El Niño and La Niña events. *J. Climate*, **13**, 2960–2972.

Chang Y-L & L-Y Oey, 2012: The Philippines-Taiwan Oscillation: Monsoon-Like Interannual Oscillation of the Subtropical-Tropical Western North Pacific Wind

System and Its Impact on the Ocean. J. Climate, 25(5), 1597-1618.

Chen, G., B. Chapron, R. Ezraty, and D. Vandemark, 2002: A global view of swell and wind sea climate in the ocean by satellite altimeter and scatterometer. *J. Atmos. Oceanic Technol.*, **19**, 1849–1859.

Chen, S., R. Wu, W. Chen, B. Yu, X. Cao, 2016: Genesis of westerly wind bursts over the equatorial western Pacific during the onset of the strong 2015–2016 El Niño. Atmos Sci Lett, 17: 384–391.

Chen, W.-B., L.-Y. Lin, J.-H. Jang, and C.-H. Chang, 2017: Simulation of Typhoon-Induced Storm Tides and Wind Waves for the Northeastern Coast of Taiwan Using a Tide-Surge-Wave Coupled Model. Water, 9, 549; doi:10.3390/w9070549.

Chia, H. H., and C. F. Ropelewski, 2002: The interannual variability in the genesis location of TCs in the northwest Pacific. *J. Climate*, **15**, 2934–2944.

Chu, P.-S., and J. Wang, 1997: Tropical cyclone occurrences in the vicinity of Hawaii: Are the differences between El Niño years significant? *J. Climate*, **10**, 2683–2689.

Collins, M., 2000: Understanding uncertainties in the response of ENSO to greenhouse warming. *Geophys. Res. Lett.*, **27**, 3509–3513.

Cox, A. T., and V. R. Swail, 2001: A global wave hindcast over the period 1958–1997: Validation and climate assessment, *J. Geophys. Res.*, **106**(C2), 2313–2329, doi:10.1029/2001JC000301.

Cotton, P. D., and D. J. T. Carter, 1994, Cross calibration of TOPEX, ERS-1, and Geosat wave heights, *J. Geophys. Res.*, **99**, 25,025– 25,033, Correction, *J. Geophys. Res.*, 100, 7095, 1995.

Donelan, M., M. Skafel, H. Graber, P. Liu, D. Schwab, and S. Venkates (1992), On the growth of wind-generated waves. *Atmos.–Ocean,* 30**,** 457–478.

Donelan, M. A. et al (2012), Modeling waves and wind stress, *J. Geophys. Res.*, 117, C00J23, doi:10.1029/2011JC007787.

Elsner, J. B., and K. B. Liu, 2003: Examining the ENSO-typhoon hypothesis. *Climate Res.*, **25**, 43–54.

Emanuel, K. A., 1991: The theory of hurricanes. Annu. Rev. Fluid Mech, 23, 179–196.

Fan, Y., S.-J. Lin, S. M. Griffies, and M. A. Hemer, 2014: Simulated global swell and wind-sea climate and their responses to anthropogenic climate change at the end of the twenty-first century. *J. Climate*, **27**, 3516–3536, doi:https://doi.org/10.1175/JCLI-D-13-00198.1.

Fu, D., P. Chang, and C. M. Patricola, 2017: Intrabasin variability of East Pacific tropical cyclones during ENSO regulated by central American gap winds, *Sci. Rep.*, **7**(1), 1658, doi:10.1038/s41598-017-01962-3.

Gray, W. M., 1984: Atlantic seasonal hurricane frequency. Part I: El Niño and 30 mb quasi-biennial oscillation influences. *Mon. Wea.Rev.*, **112**, 1649–1668.

Gulev, S. K., and V. Grigorieva, 2006: Variability of the winter wind waves and swell in the North Atlantic and North Pacific as revealed by the voluntary observing ship data. *J. Climate*, **19**, 5667–5685.

Gulev, S. K. and L. Hasse, 1999: Changes of wind waves in the North Atlantic over the last 30 years. *Int. J. Climatol.*, **19**: 1091–1117, doi:10.1002/(SICI)1097-0088(199908)19:10<1091::AID-JOC403>3.0.CO;2-U.

Harr, P. A., and R. L. Elsberry, 1991: Tropical cyclone track characteristics as a function of large-scale circulation anomalies. *Mon. Wea. Rev.*, **119**, 1448–1468.

Harr, P. A., and R. L. Elsberry, 1995: Large-scale circulation variability over the tropical western North Pacific. Part I: Spatial patterns and tropical cyclone characteristics. *Mon. Wea. Rev.*, **123**, 1225–1246.

Ho, C.-H., J.-H. Kim, J.-H. Jeong, H.-S. Kim, and D. Chen,2006: Variation of tropical cyclone activity in the South Indian Ocean: El Niño– Southern Oscillation and Madden-Julian Oscillation effects, *J. Geophys. Res.*, **111**, D22101, doi:10.1029/2006JD007289.

Holland, G. J., J. I. Belanger, and A. Fritz, 2010: A revised model for radial profiles of hurricane winds. Mon. Wea. Rev., 138, 4393–4406.

Holthuijsen, L. H., M. D. Powell, and J. D. Pietrzak (2012), Wind and waves in extreme hurricanes. *J. Geophys. Res*., 117, C09003.

Huang, W.-K. and J.-J. Wang, 2015: Typhoon damage assessment model analyses in Taiwan. Nature Hazards, 79, 1, 497-510.

Huang, S-M and L.-Y. Oey, 2018: Land-falling typhoons are controlled by the meridional oscillation of the Kuroshio Extension. Climate Dyn., 50(320), 1-13. https://doi.org/10.1007/s00382-018-4295-z.

Hwang, P. A., and D. W. Wang (2004), Field measurements of duration limited growth of wind-generated ocean surface waves at young stage of development. *J. Phys. Oceanogr*., 34, 2316–2326.

Hwang, P. A., and M. A. Sletten, 2008: Energy dissipation of windgenerated waves and whitecap coverage. J. Geophys. Res., 113, C02012, doi:10.1029/2007JC004277; Corrigendum, 114, C02015, doi:10.1029/2008JC005244.

Hwang, P. A., 2016: Fetch- and duration-limited nature of surface wave growth inside tropical cyclones: With applications to air-sea exchange and remote sensing. *J. Phys. Oceanogr.*, **46**, 41–56, doi:https://doi.org/10.1175/JPO-D-15-0173.1.

Hwang, P. A., H. García-Nava, and F. J. Ocampo-Torres, 2011: Observations of wind wave development in mixed seas and unsteady wind forcing, *J. Phys. Oceanogr.*, **41**, 2340–2359, doi:10.1175/2011JPO-D-11-044.1.

Hwang, P. A., and E. J. Walsh, 2016: Azimuthal and radial variation of wind-generated surface waves inside tropical cyclones. *J. Phys. Oceanogr.*, **46**, 2605–2621, doi:https://doi.org/10.1175/JPO-D-16-0051.1.

Jakobsen, F. and H. Madsen, 2004: Comparison and further development of parametric tropical cyclone models for storm surge modelling. J. Wind Eng. Ind. Aerodyn. 92, 375 – 391.

Knapp, K. R., M. C. Kruk, D. H. Levinson, H. J. Diamond, and C. J. Neumann, 2010: The International Best Track Archive for Climate Stewardship (IBTrACS): Unifying tropical cyclone best track data, *Bull. Am. Meteorol. Soc.*, **91**, 363–376.

Knaff, J. A., C. R. Sampson, M. DeMaria, T. P. Marchok, J. M. Gross, and C. J. McAdie, 2007: Statistical tropical cyclone wind radii prediction using climatology and persistence. Wea. Forecasting, 22, 781–791.

Kushnir, Y., V. J. Cardon, J. G. Greenwood, and M. A. Cane, 1997:The recent increase in North Atlantic wave heights. *J. Climate*, **10**, 2107–2113.

Kuleshov, Y., L. Qi, R. Fawcett, and D. Jones, 2008: On tropical cyclone activity in the Southern Hemisphere: Trends and the ENSO connection, *Geophys. Res. Lett.*, **35**, L14S08, doi:10.1029/2007GL032983.

Kuleshov Y, Chane Ming F, Qi L, Chouaibou I, Hoareau C, Roux F. 2009. Tropical cyclone genesis in the Southern Hemisphere and its relationship with the ENSO. *Annales Geophysicae*, **27**: 2523–2538.

Kundu, P., J. S. Allen, and R. L. Smith, 1975: Modal decomposition of the velocity field near the Oregon coast. J. Phys. Oceanogr., 5, 683–704.

Kutzbach, J.E., 1967. "Empirical eigenvectors of sea-level pressure, surface temperature, and precipitation complexes over North America." *J. of Applied Meteorology,* 6(5), 791-802.

Lander, M. A., 1994: An exploratory analysis of the relationship between tropical storm formation in the western North Pacific and ENSO. *Mon. Wea. Rev.*, **122**, 636–651.

Lander, M. A., 1996: Specific tropical cyclone tracks and unusual tropical cyclone motions associated with a reverse-oriented monsoon trough in the western North Pacific. *Wea. Forecasting*, **11**, 170–186.

Landsea, C. W., 2000: El Niño–Southern Oscillation and the seasonal predictability of tropical cyclones. El Niño: Impacts of Multiscale Variability on Natural Ecosystems and Society, H. F. Diaz and V. Markgraf, Eds., 149–181.

Lau, N.-C., and M. J. Nath, 2003: Atmosphere–Ocean Variations in the Indo-Pacific Sector during ENSO Episodes, J. Clim., **16**, 3-20.

Liang, A. (T.-Y.), L. Oey, S. Huang, and S. Chou (2017), Long-term trends of typhoon-induced rainfall over Taiwan: In situ evidence of poleward shift of typhoons in western North Pacific in recent decades, J. Geophys. Res. Atmos., 122(5), 2750-2765. doi:10.1002/2017JD026446.

Lin, X.-H., L.-Y. Oey & D.-P. Wang, 2007: Altimetry and drifter assimilations of Loop Current and eddies. JGR, 112(C5), C05046, doi:10.1029/2006JC003779, 2007.

Lin, YC, L.-Y. Oey, J.Wang & K.K. Liu, 2016: Rossby waves and eddies observed at a temperature mooring in northern South China Sea. J. Phys. Oceangr, 46(2), 517-535. DOI: 10.1175/JPO-D-15-0094.1.

Lin, Y.-C., and L.-Y. Oey, 2016: Rainfall-enhanced blooming in typhoon wakes. Scientific Reports, 6, 31310. DOI: 10.1038/srep31310.

Liu, K. S., and J. C. L. Chan, 2012: Interannual variation of Southern Hemisphere tropical cyclone activity and seasonal forecast of tropical cyclone number in the Australian region. *Int. J. Climatol.*, **32**, 190–202, doi:10.1002/joc.2259.

Madden, R. A., and P. R. Julian, 1971: Detection of a 40–50 day oscillation in the zonal wind. J. Atmos. Sci., 28, 702–708.

Madden, R.A. and P.R. Julian, 1972: Description of global-scale circulation cells in the tropics with a 40- 50 day period. J. Atmos. Sci., 29, 1109-1123.

Mellor, G. L., M. A. Donelan, and L-Y. Oey, 2008: A surface wave model for coupling with numerical ocean circulation models. J. Atmos. Oceanic Technol., 25, 1785–1807.

Moon, I-J, I Ginis and T. Hara (2003), Numerical simulation of sea surface directional wave spectra under hurricane wind forcing. *J. Phys. Oceanogr.* 33, 1680-1706.

Munk, W. H., G. R. Miller, F. E. Snodgrass, and N. F. Barber, 1963: Directional recording of swell from distant storms. *Philos. Trans. Roy. Soc. London*, A255, 505–584.

Nakamura, H., Sampe, T., Tanimoto, Y., and Simpo, A., 2004, in Earth's Climate: The Ocean-Atmosphere Interaction Geophysical Monograph 147, pp. 329-346.

Needham, H. F., B. D. Keim, and D. Sathiaraj, 2015: A review of tropical cyclone-generated storm surges: Global data sources, observations, and impacts. Rev. Geophys. 53, 545–591.

Nicholls, N., 1984: The southern oscillation, sea-surface temperature, and internannual fluctuations in Australian tropical cyclone activity. *J. Climatol.*, **4**, 661–670.

Nicholls, N., 1985: Predictability of interannual variations in Australian seasonal tropical cyclone activity. *Mon. Wea. Rev.*, **113**, 1144– 1149.

North, G. R., T. L. Bell, and R. F. Cahalan, 1982: Sampling errors in the estimation of empirical orthogonal functions. *Mon. Wea. Rev.*, **110,** 699–706.

Oey L-Y, 2008: Loop Current and Deep Eddies. J. Phys. Oceanogr. 38(7), 1426-1449.

Oey, L-Y., T. Ezer, and W. Sturges, 2004: Modeled and observed empirical orthogonal functions of currents in the Yucatan Channel, Gulf of Mexico. Journal of

Geophysical Research, 109(C08), C08011, doi: 10.1029/2004JC002345.

Oey, L.-Y., T. Ezer, D.-P. Wang, S.-J. Fan, and X.-Q. Yin, 2006: Loop current warming by Hurricane Wilma. *Geophys. Res. Lett.*, **33**, L08613, doi:10.1029/2006GL025873.

Oey et al. 2007: Hurricane-induced motions and interaction with ocean currents, CSR, 27(9), 1249-1263. doi:10.1016/j.csr.2007. 01.008.

Oey, L.-Y. and S. Chou, 2016: Evidence of rising and poleward shift of storm surge in western North Pacific in recent decades. *J. of Geophys. Res. Oceans.* DOI: 10.1002/2016JC011777.

Oey, L.-Y., T. Ezer, C. Hu, and F. Muller-Karger, 2007: Baroclinic tidal flows and inundation processes in Cook Inlet, Alaska: numerical modeling and satellite observations, *Ocean Dyn.*, **57**, 205–221.

Oey, L-Y., Chang Y-L, Sun S.B & Lin X.H, 2009: Topocaustics. Ocean Modelling, 29(4), 277-286.

Oey, L.-Y., M.-C. Chang, Y.-L. Chang, Y.-C. Lin, and F.-H. Xu, 2013: Decadal warming of coastal China Seas and coupling with winter monsoon and currents. Geophys. Res. Lett., 40, 6288–6292, doi:10.1002/2013GL058202.

Oey and Chao 2016: Evidence of rising and poleward shift of storm surge in western North Pacific in recent decades. Journal of Geophysical Research–Oceans, 121(7), 5181-5192, DOI: 10.1002/2016JC011777.

Powell, M. D., P. J. Vickery, and T. A. Reinhold, 2003: Reduced drag for high wind speeds in TCs, *Nature*, **422**, 279–283.

Ramsay, H. A., S. J. Camargo, and D. Kim, 2012: Cluster analysis of tropical cyclone tracks in the Southern Hemisphere. *Climate Dyn.*, **39**, 897–917, doi:10.1007/s00382-011-1225-8.

Sandwell, D. T., and R. W. Agreen, 1984: Seasonal Variation in Wind Speed and Sea

State from Global Satellite Measurements, *J. Geophys. Res.*, **89**, 2041-2051.

Saji, N.H., B.N. Goswami, P.N. Vinayachandran and T. Yamagata, 1999: A dipole mode in the tropical Indian Ocean. Nature, 401, 360-363.

Semedo, A., K. Suselj, A. Rutgersson, and A. Sterl, 2011: A global view on the wind sea and swell climate and variability from ERA-40. J. Clim. 24, 1461–1479.

Shaman, J., Esbensen, S. K., & Maloney, E. D., 2009: The dynamics of the ENSO–Atlantic hurricane teleconnection: ENSO-related changes to the North African–Asian jet affect Atlantic basin tropical cyclogenesis. *J. of Climate*, **22**(9), 2458-2482.

Snodgrass, F. E., G. W. Groves, K. F. Hasselmann, G. R. Miller, W. H. Munk, and W. M. Powers, 1966: Propagation of swell across the Pacific. *Philos. Trans. Roy. Soc. London*, A259, 431–497.

Solow, A., and N. Nicholls, 1990: The relationship between the Southern Oscillation and tropical cyclone frequency in the Australian region. *J. Climate*, **3**, 1097–1101, doi:10.1175/1520-0442(1990)003,1097:TRBTSO.2.0.CO;2.

Stephens, S. A., and D. L. Ramsay, 2014: Extreme cyclone wave climate in the southwest Pacific Ocean: Influence of the El Niño Southern Oscillation and projected climate change. *Global Planet Change*, **123**, 13–26, doi:10.1016/j.gloplacha.2014.10.002.

Sterl, A., G. J. Komen, and P. D. Cotton, 1998: Fifteen years of global wave hindcasts using winds from the European Centre for Medium-Range Weather Forecasts reanalysis: Validating the reanalyzed winds and assessing the wave climate, *J. Geophys. Res.*, **103**(C3), 5477–5492, doi:10.1029/97JC03431.

Sun, J, and Lie-Yauw Oey, 2015: The influence of ocean on Typhoon Nuri (2008). Monthly Weather Review, 143(11), 4493-4513, DOI:10.1175/MWR-D-15-0029.1.

Sun, J. R., L.-Y. Oey, R. Chang, F. Xu, and S. M. Huang, 2015: Ocean response to typhoon Nuri (2008) in western Pacific and South China Sea, *Ocean Dyn.*, **65**, 735–749, doi:10.1007/s10236-015-0823-0.

Sun, J. R., L. Oey, F.-H. Xu, and Y.-C. Lin, 2017: Sea level rise, surface warming, and the weakened buffering ability of South China Sea to strong typhoons in recent decades. Sci. Rep., 7, 7418, doi:10.1038/s41598-017-07572-3.

Tamura, H., Y. Miyazawa, and L.-Y. Oey, 2012: The Stokes drift and wave induced-mass flux in the North Pacific, J. Geophys. Res., 117, C08021, doi:10.1029/2012JC008113.

Tang, B. H., and Neelin, J. D., 2004, ENSO influence on Atlantic hurricanes via tropospheric warming, *Geophys. Res. Lett.*, **31**, L24204, doi:10.1029/2004GL021072.

Thomas, B. R., E. C. Kent, V. R. Swail, and Berry, D. I., 2008: Trends in ship wind speeds adjusted for observation method and height. *Int. J. Climatol.*, **28**: 747–763, doi:10.1002/joc.1570.

Toba, Y. (1972), Local balance in the air-sea boundary processes I. On the growth process of wind waves. *J. Oceanogr. Soc. Jpn.*, 28, 109-120.

Tolman, H. L., 1991: Effects of tides and storm surges on North Sea wind waves. J. Phys. Oceanogr. 21, 766-791.

Tolman, H. L., and D. V. Chalikov (1996), Source terms in a third-generation wind wave model, J. Phys. Oceanogr., 26, 2497–2518.

Tolman, H. L. (2002), User manual and system documentation of WAVEWATCH-III version 2.22, Tech. Note, 222, 133 pp., Mar. Model. and Anal. Branch, Natl. Cent. for Environ. Predict., Natl. Weather Serv., NOAA, Camp Springs, Md.

Toma, V. and P. J. Webster, 2010: Oscillations of the intertropical convergence zone and the genesis of easterly waves. I Theory and diagnostics. *Clim. Dyn.*, **34**, 587-604.

Vikebø F, Furevik T, Furnes G, Kvamstø NG, Reistad M., 2003: Wave height variations in the North Sea and on the Norwegian Continental Shelf, 1881–1999. *Cont. Shelf Res.*, 23, 251–263, doi:10.1016/S0278-4343(02)00210-8.

WAVEWATCH III Development Group, 2016: User manual and system documentation of WAVEWATCH III version 5.16, *Tech. Note 329*, 326 pp., NOAA/NWS/NCEP/MMAB, College Park, Md.

Wang, B., Z. W. Wu, J. P. Li, J. Liu, C.-P. Chang, Y. H. Ding, and G. X. Wu, 2008: How to measure the strength of the East Asian summer monsoon. *J. Climate*, **21**, 4449–4463, doi: 10.1175/2008JCLI2183.1.

Wang, J. and L.-Y. Oey, 2014: Inter-annual and decadal fluctuations of the Kuroshio in East China Sea and connection with surface fluxes of momentum and heat, Geophys. Res. Lett., 41(23), doi:10.1002/2014GL062118.

Wang, Jia and L.-Y. Oey, 2016: Seasonal exchanges of Kuroshio and shelf waters and their impacts on the shelf currents of the East China Sea. Journal of Physical Oceanography, 46(5), 1615-1632. DOI: 10.1175/JPO-D-15-0183.1.

Wentz, F. J., J. Scott, R. Hoffman, M. Leidner, R. Atlas, and J. Ardizzone. 2016: Cross-Calibrated Multi-Platform Ocean Surface Wind Vector Analysis Product V2, 1987 - ongoing. Research Data Archive at the National Center for Atmospheric Research, Computational and Information Systems Laboratory. http://rda.ucar.edu/datasets/ds745.1/. Accessed 09 Jan 2017

Wilcoxon, F., 1945: Individual comparisons by ranking methods. *Biometrics Bulletin*. 1 (6): 80–83. doi:10.2307/3001968.

Woolf D. K., Challenor P. G., and Cotton P. D., 2002: The variability and predictability of North Atlantic wave climate. *J. of Geophys. Res.*, **107**(C10):9.1–9.14. doi: 10.1029/2001JC001124.

Xie, S. P., H. Annamalai, F. A. Schott, and J. P. McCreary Jr., 2002: Structure and mechanism of South Indian Ocean climate variability, J.Clim., 15, 864–878.

Xu, F.-H., L.-Y. Oey, 2011: The Origin of Along-Shelf Pressure Gradient in the Middle Atlantic Bight. J. Phys. Oceanogr 41(9), 1720-1740.

Xu, FH and Lie-Yauw Oey, 2015: Seasonal SSH Variability of the Northern South China Sea. J. Phys. Oceanogr., 45(6), 1595–1609. doi: http://dx.doi.org/10.1175/JPO-D-14-0193.1.

Yang, R.-Y., Y.-C. Wu, H.-H. Hwung, J.-Y. Liou, and I. V. Shugan,, 2010: Current countermeasure of beach erosion control and its application in Taiwan. Ocean & Coastal Manage., **53**, 552-561.

Young, I. R., 1988: Parametric hurricane wave prediction model. *J. Waterw. Port Coastal Ocean Eng.*, **114**, 637-652, doi:10.1061/(ASCE)0733-950X(1988)114:5(637).

Young, I. R., 1998: Observations of the spectra of hurricane generated waves. *Ocean Eng.*, 25, 261–276, doi:10.1016/S0029-8018(97)00011-5.

Young, I. R., 1999: Seasonal variability of the global ocean wind and wave climate. *Int. J. Climatol.*, 19, 931. doi:10.1002/(SICI)1097-0088(199907)19:9<931::AID-JOC412>3.0.CO;2-O.

Young, I. R., 2003: A review of the sea state generated by hurricanes. *Mar. Struct.*, **16**, 201–218, doi:10.1016/S0951-8339(02)00054-0.

Young, I. R., 2006: Directional spectra of hurricane wind waves. *J. Geophys. Res.*, **111**, C08020, doi:10.1029/2006JC003540.

Young, I. R., and J. Vinoth, 2013: An "extended fetch" model for the spatial distribution of tropical cyclone wind-waves as observed by altimeter. *Ocean Eng.*, **70**, 14–24, doi:10.1016/j.oceaneng.2013.05.015.

Young, I.R., Zieger, S., Babanin, A.V., 2011: Global trends in wind speed and wave height. *Science*, **332** (6028), 451–455.

Zhang L., & Oey, L. 2019a: Young ocean waves favor the rapid intensification of tropical cyclones - a global observational analysis, Mon. Wea. Rev. 147, 311-328. (https://journals.ametsoc.org/doi/full/10.1175/MWR-D-18-0214.1).

Zhang, L., & Oey, L. 2019b: An observational analysis of ocean surface waves in tropical cyclones in the western North Pacific Ocean. Journal of Geophysical Research: Oceans, 124, 184–195. https://doi.org/10.1029/2018JC014517.

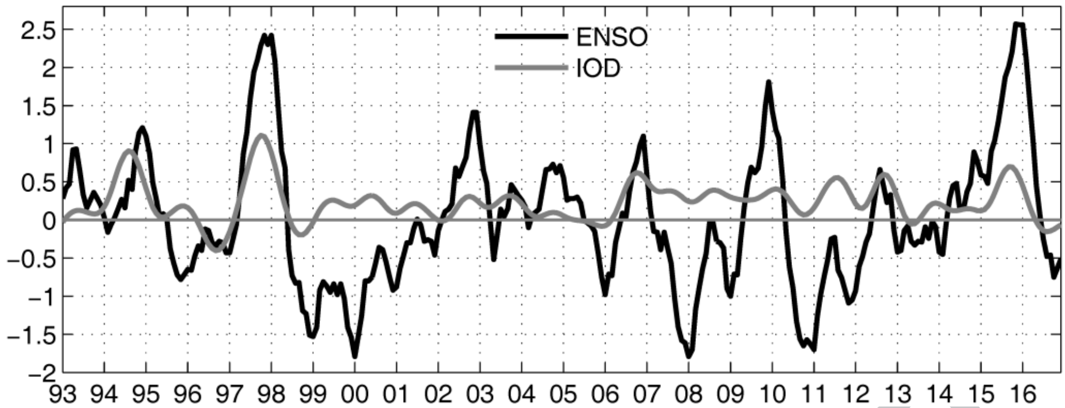

Figure 1: ENSO (black) and IOD (grey) indices from Jan 1993 to Dec 2016.

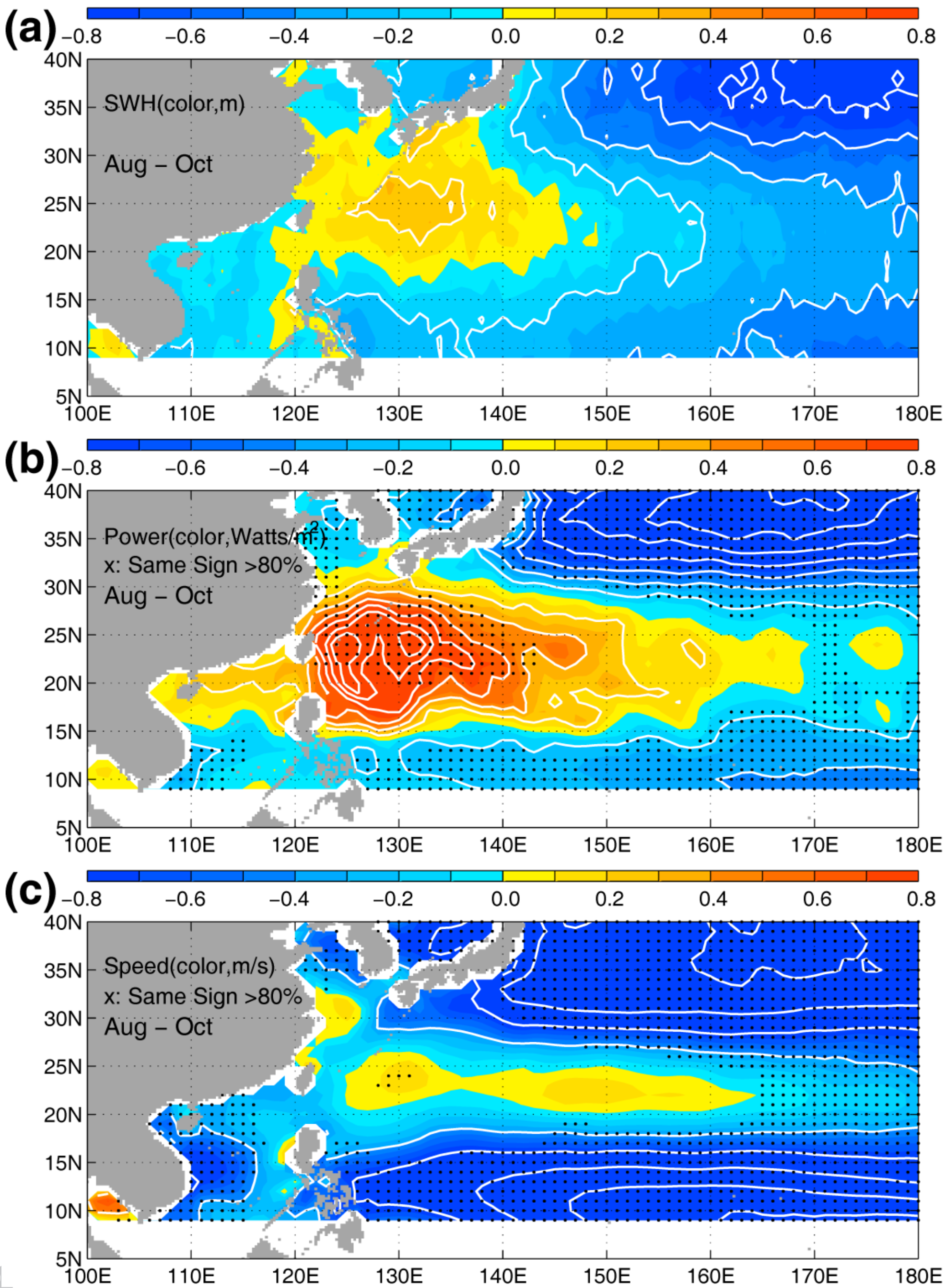

Figure 2: August to October composites of (a) SWH [m], (b) wind power [Watts m^{-2}], and (c) wind speed [m s^{-1}] anomalies (color shading and white contours) from 1993 to 2016. Dots (b & c) show where 80% of the grid values of wind power or speed in 5°×5° squares are of the same the sign as the sign of SWH.

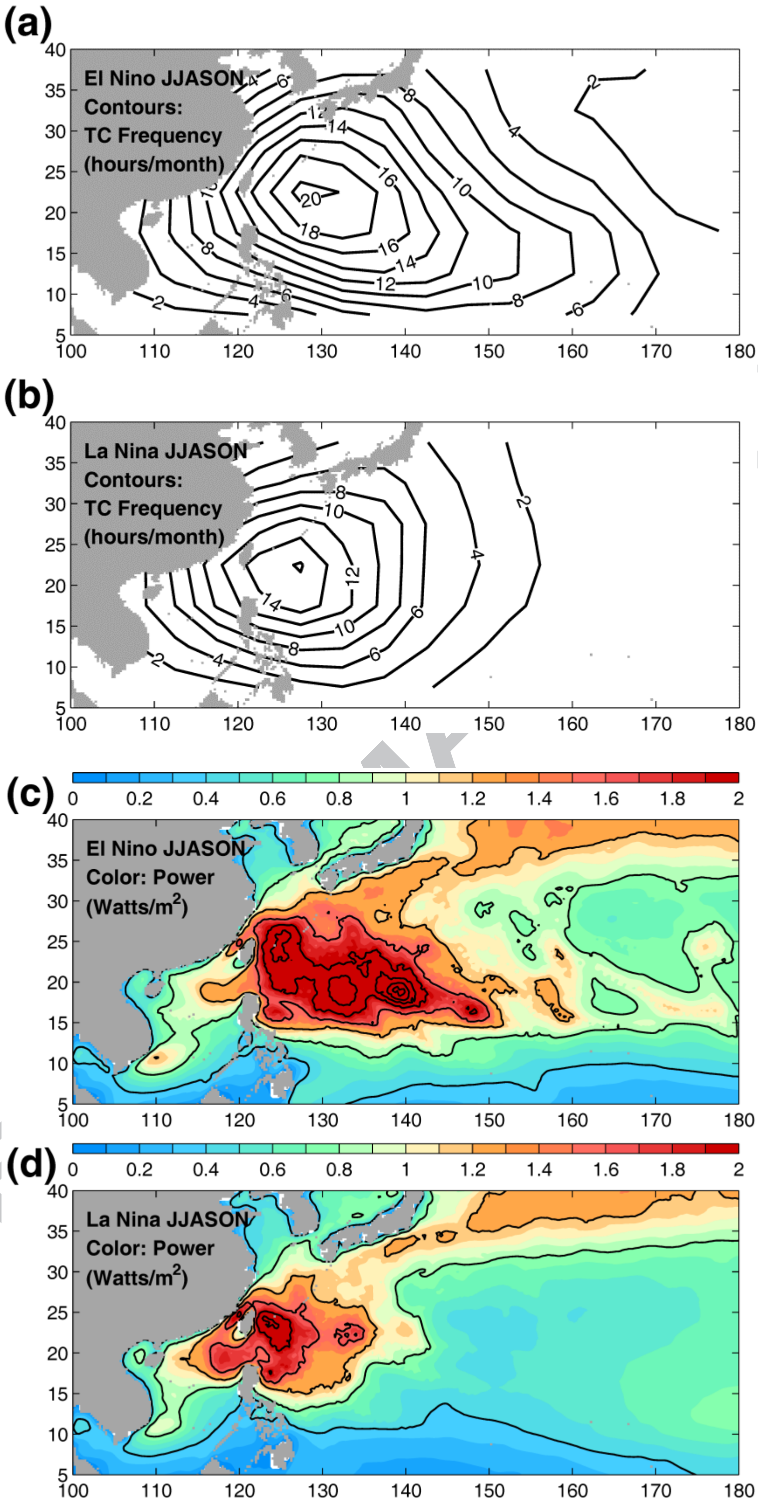

Figure 3. Composites of (a & b) TC visitation frequency [hours/month] and (c & d) wind power [Watts/m^2] from June to November during El Niño (a & c) and La Niña (b & d).

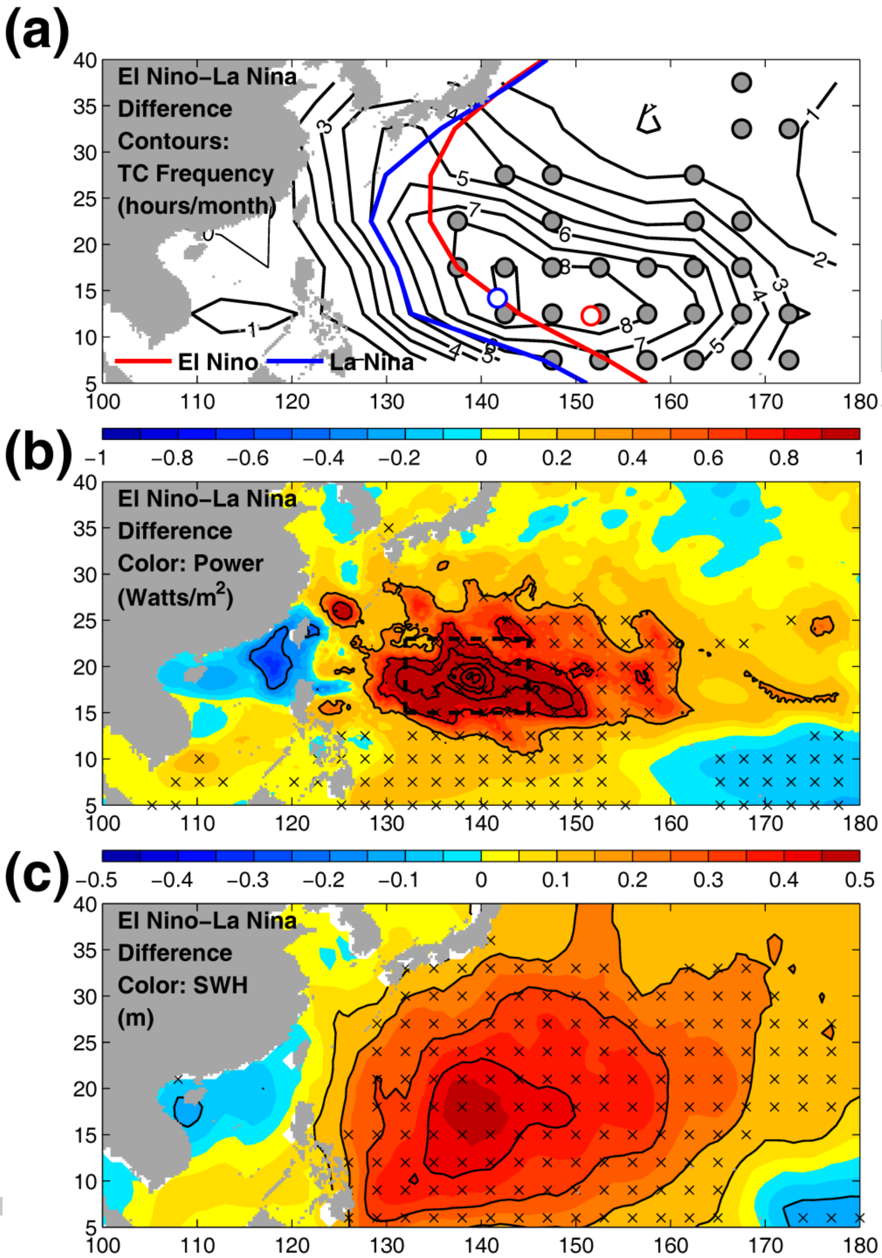

Figure 4 Composite differences (El Niño *minus* La Niña) of (a) TC frequency [hours month^{-1}], (b) wind power [Watts m^{-2}] and (c) significant wave height [m]. Grey-filled circles and crosses indicate significant differences at the 95% confidence level according to the two-sided Wilcoxon rank sum test. In (a), mean TC tracks and genesis locations during El Niño (red) and La Niña (blue) are also plotted [see Lin and Oey 2016; Oey and Chou 2016; Liang et al. 2017].

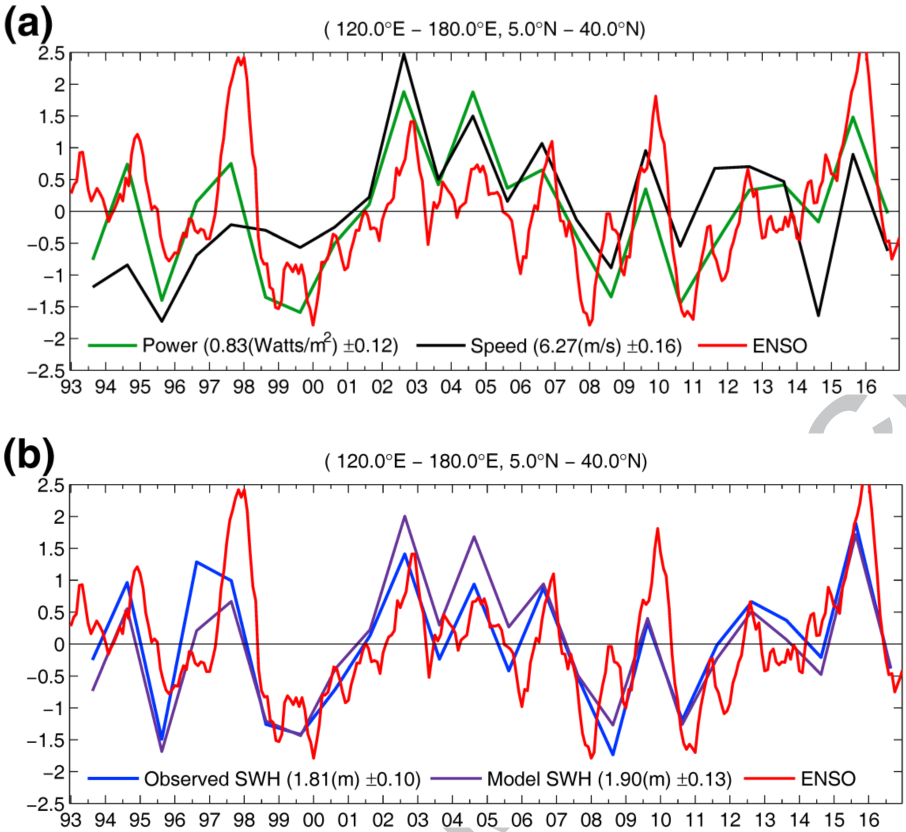

Figure 5 Yearly variations of (a) wind power [Watts m^{-2}] (green) and speed [m s^{-1}] (black), and (b) observed (blue) and model (purple) SWHs [m], all averaged for the TC season JJASON and in the western North Pacific: 120°E–180°E, 5°N–40°N. The means were removed and the time series were normalized by the standard deviations. Means and standard deviations are shown in the legends across the bottom. The correlations of power and speed with SWHs, as well as with ENSO are: Corr(Power,ObsSWH) = 0.89, Corr(Speed,ObsSWH) = 0.59, Corr(Power,ModelSWH) = 0.99, Corr(Speed,ModelSWH) = 0.79, and Corr(Power,ENSO) = 0.75, all at 99.9% confidence level, and Corr(Speed,ENSO) = 0.34 at 90% confidence.

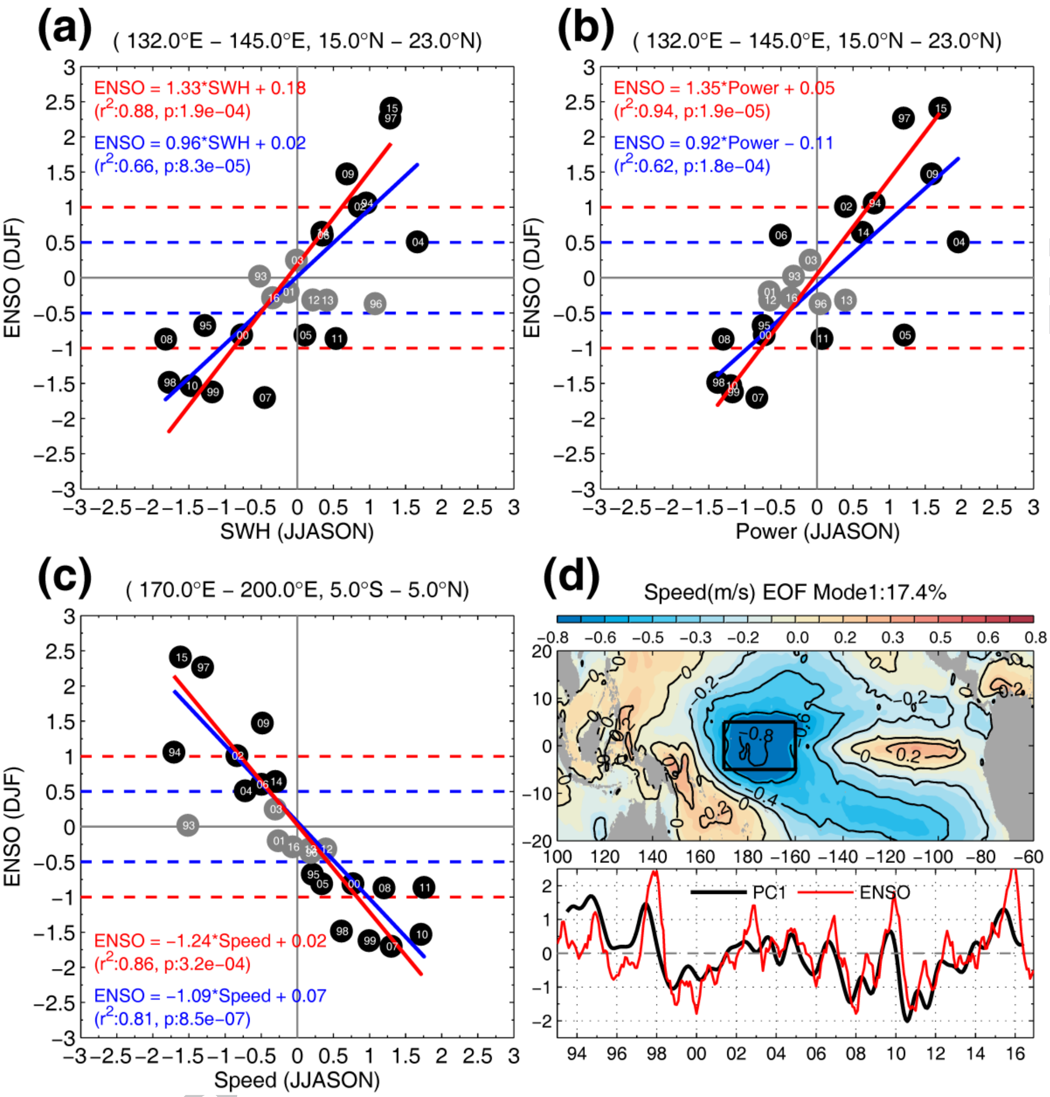

Figure 6 Regressions of December-February ENSO *vs.* June-November (a) SWH [m] and (b) wind power [Watts m^{-2}] averaged over the *subtropical* western North Pacific (see panel title, dashed rectangle of Fig.4b), and (c) *equatorial* wind speed [m s^{-1}] within the Niño-4 (dashed rectangle in (d)) where the dominant wind speed EOF is highest, as shown in (d): eigenvector (upper subpanel) and principal component time series (lower subpanel). In (a-c), blue indicates moderate and higher-intensity ENSO events, |ENSO| ≥ 0.5, and red indicates strong ENSO events, |ENSO| ≥ 1.

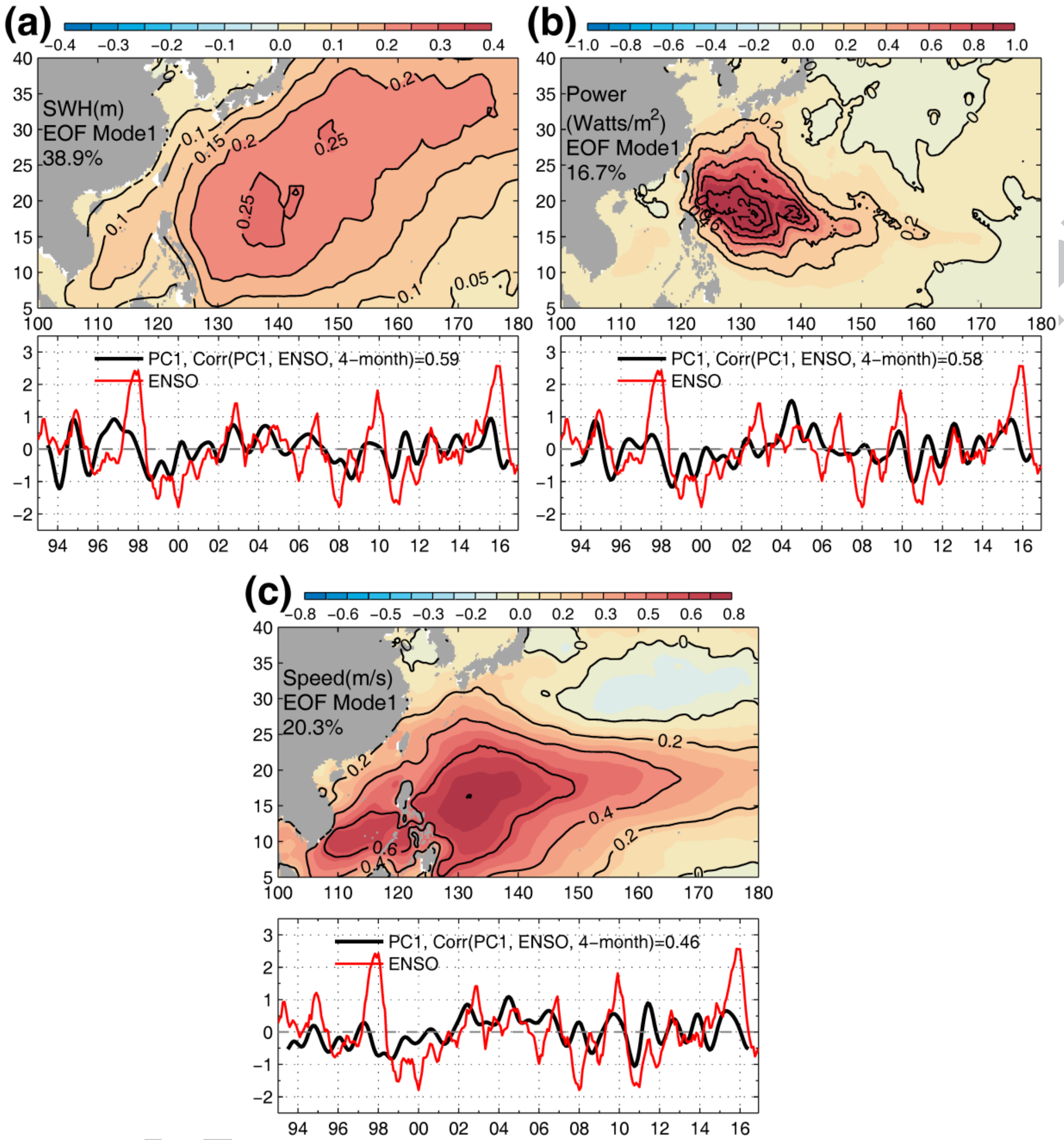

Figure 7: First EOF modes of (a) observed SWH [m], (b) wind power [Watts m^{-2}], and (c) wind speed [m s^{-1}]. Upper subpanels show the eigenvectors and lower subpanels show the principal components (black lines). Red lines in lower subpanels are the ENSO index. The lag-correlation *Corr(A, B, lag)* in the lower subpanels show maximum lagged correlations with *A* leading (lagging) *B* when *lag* is positive (negative), significant at the 95% confidence level.

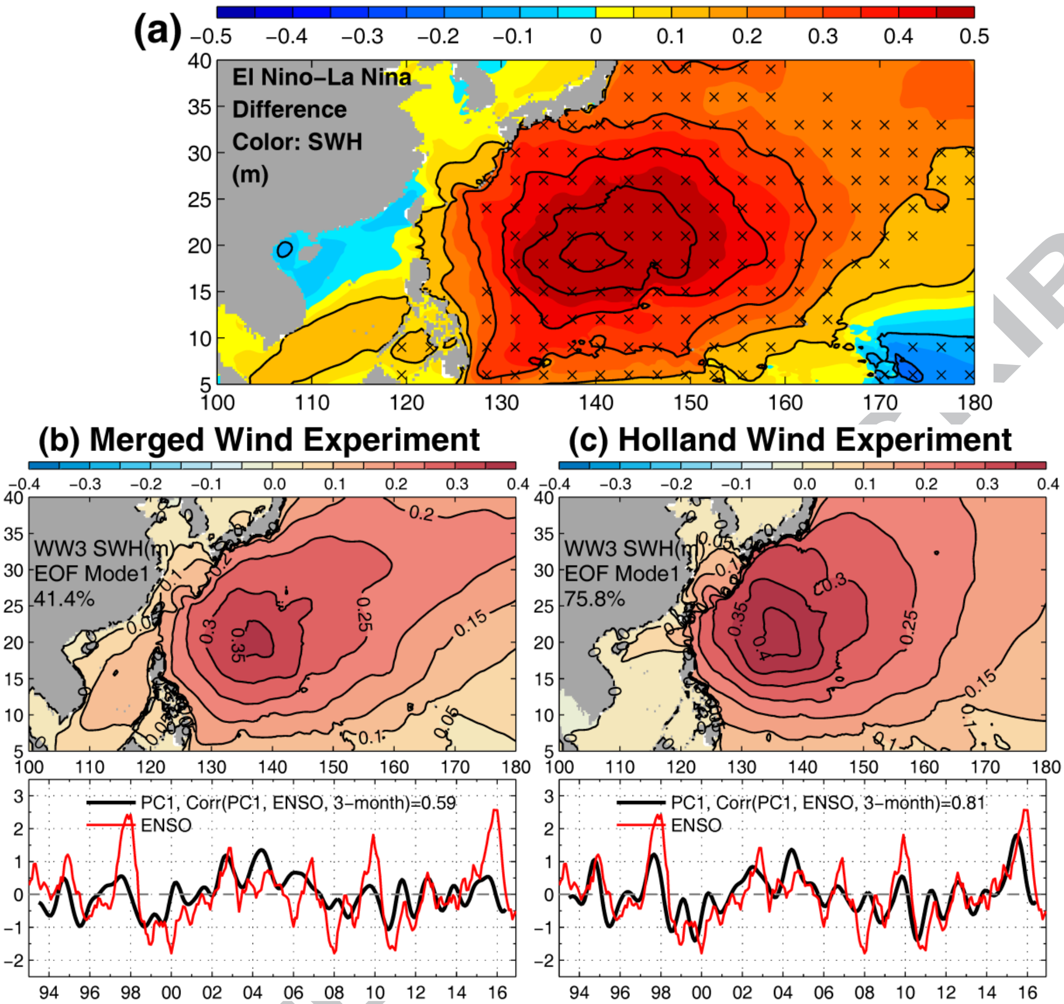

Figure 8 (a) Composite difference (El Niño *minus* La Niña) of the WW3 model significant wave height [m] for the merged wind experiment, which may be compared with the observed composite difference in Fig.4c. Crosses indicate significant differences at the 95% confidence level according to the two-sided Wilcoxon rank sum test. (b & c) First EOF modes of SWH [m] for WW3 model experiments using (b) the merged wind and (c) the Holland wind. Upper subpanels show the eigenvectors and lower subpanels show the principal components (black lines). Red lines in lower subpanels are the ENSO index. The lag-correlation *Corr(A, B, lag)* in the lower subpanels show maximum lagged correlations with *A* leading (lagging) *B* when *lag* is positive (negative), significant at the 95% confidence level.

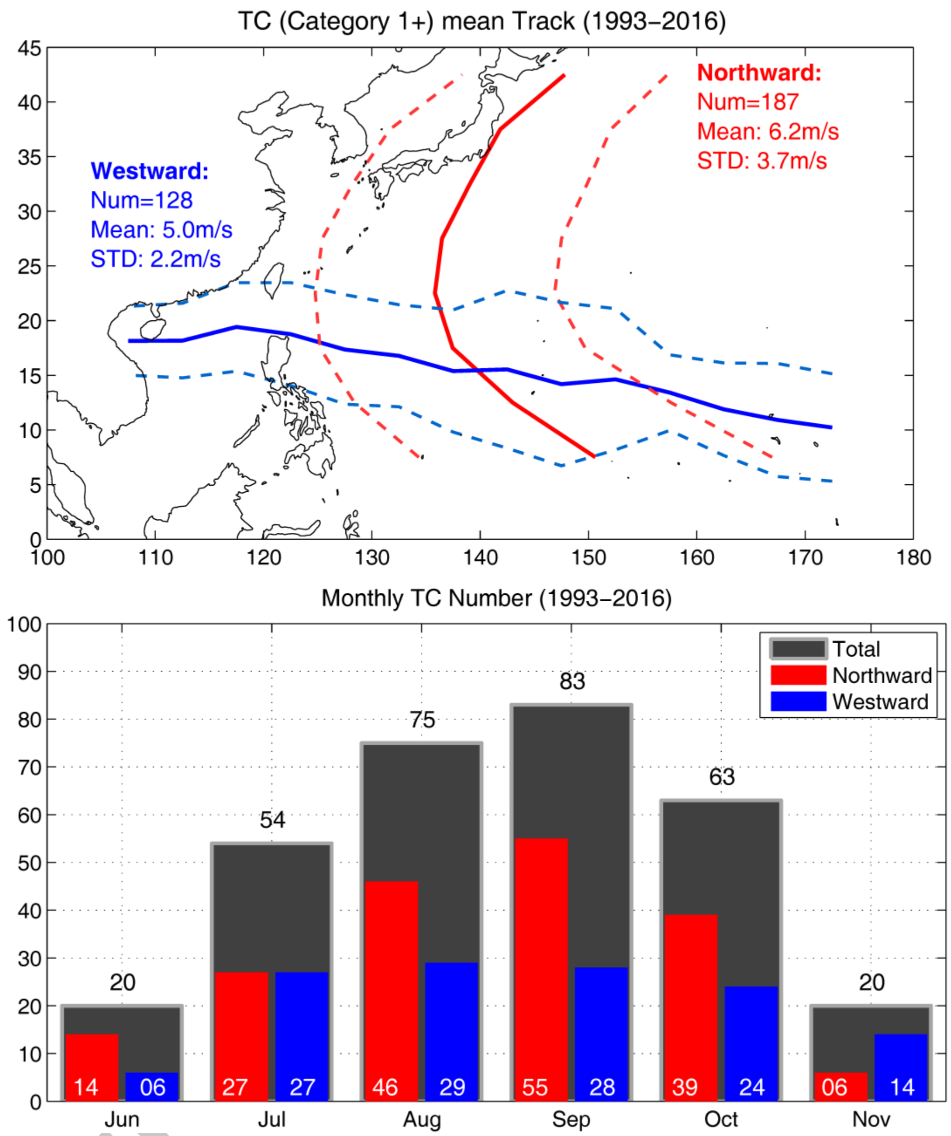

Figure 9 Mean (solid) and 1StD (dashed) tracks for northward and westward typhoons (TCs of category 1 and above) from 1993 to 2016 which are analyzed in this study (upper) [see also Lin and Oey 2016]. Monthly distributions of the total number of typhoons and their partitions into northward and westward tracks (bottom).

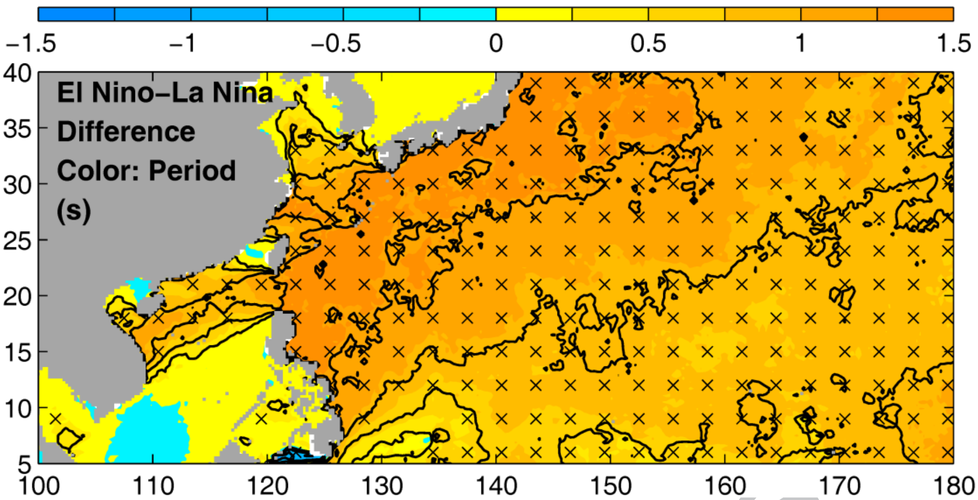

Figure 10 Composite difference (El Niño *minus* La Niña) of the WW3 model peak periods [s] for the merged wind experiment. Crosses indicate significant differences at the 95% confidence level according to the two-sided Wilcoxon rank sum test.

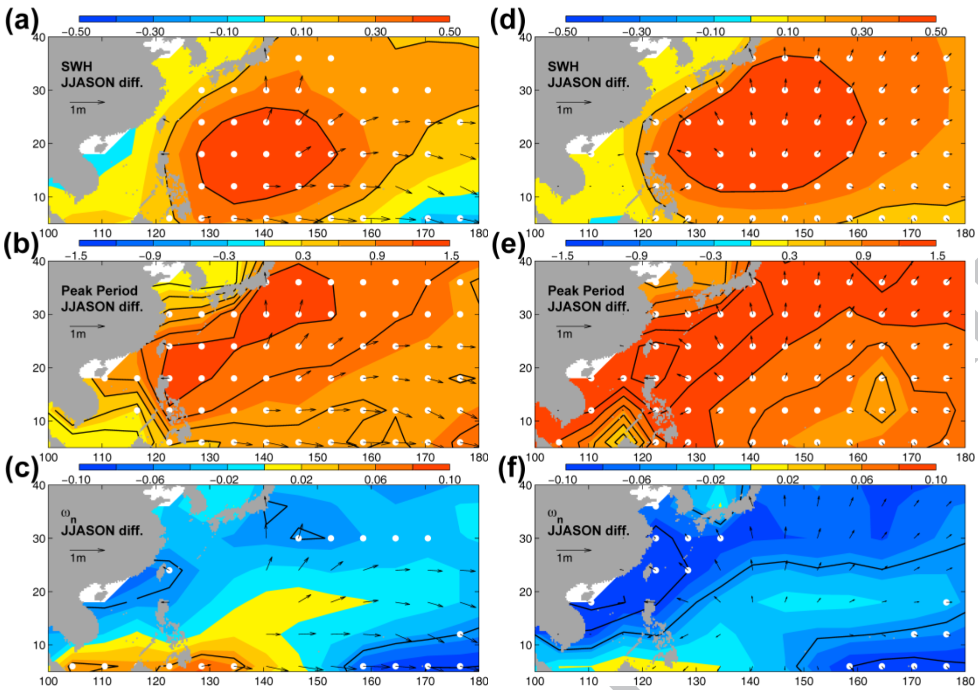

Figure 11: Composite differences between the El Niño and La Niña TC seasons of the modeled SWH [m] (a & d), peak wave period [s] (b & e), ω_n (c & f) and peak wave vectors scaled by the SWH (to emphasize the larger, e.g. TC-induced waves). Left (right) column panels a-c (d-f) are for the model forced by the merged (Holland) wind. White dots and black vectors indicate significant differences of the SWH, peak wave period, ω_n and scaled wave vectors according to the two-sided Wilcoxon rank sum test at the 95% confidence level.

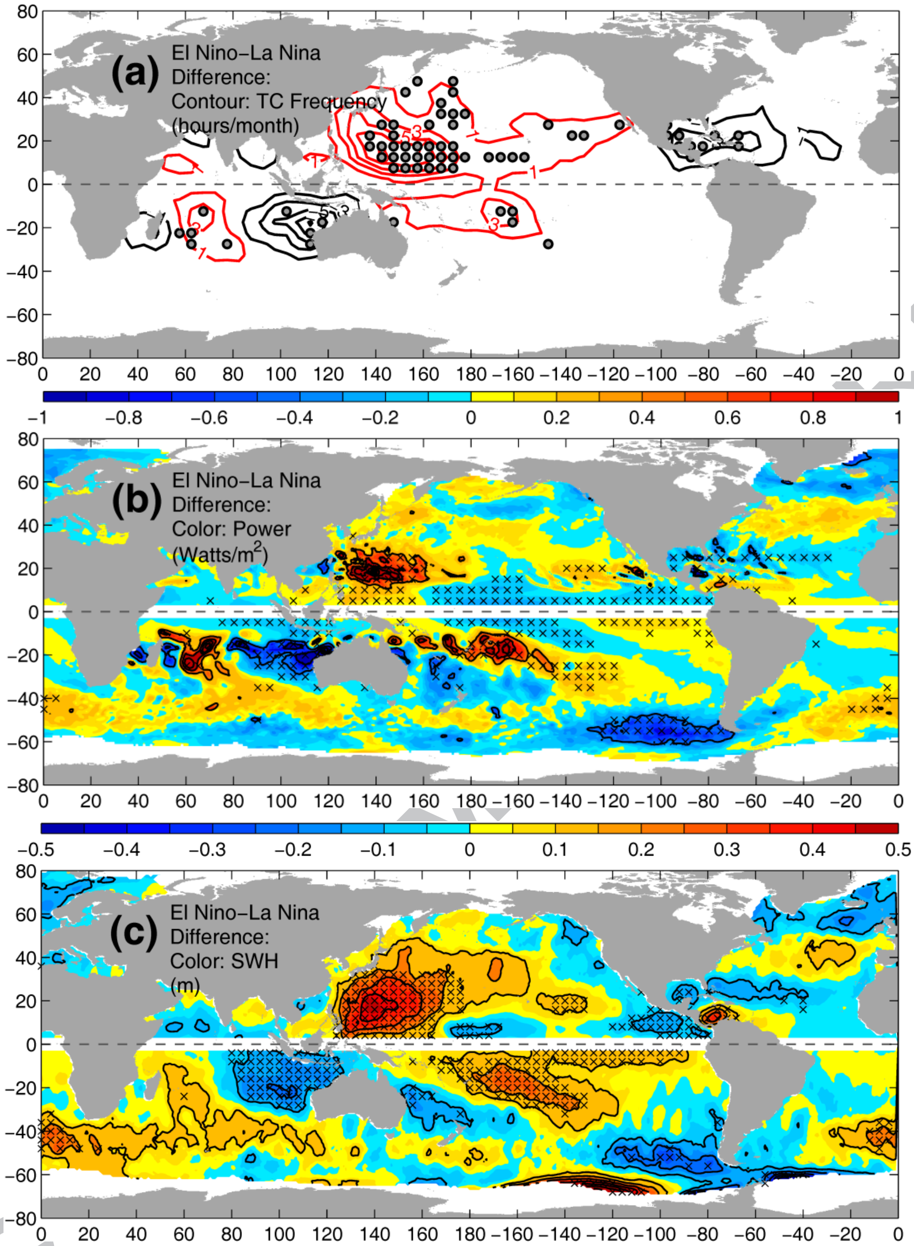

Figure 12: Composite differences (color shading) between the El Niño and La Niña TC seasons: (a) TC visitation frequency [hours/month], (b) wind power [Watts m^{-2}] and (c) observed SWH [m]. The TC season is from June to November for the northern hemisphere and from December to May in the following year for the southern hemisphere. Contours are the differences of the TC visiting frequency. Crosses and grey circles represent the significant differences of the color shading and contours, respectively, at the 95% confidence level according to the two-sided Wilcoxon rank sum test.

Highlights

Two 'faces' of ENSO-induced surface waves during the tropical cyclone season

Yuchun Lin[1], Lie-Yauw Oey[1*], and Alejandro Orfila[2]
1: National Central University, Taiwan
2: Instituto Mediterráneo de Estudios Avanzados, Spain

*Corresponding Author: lyooey@gmail.com

This study represent advances in cross-disciplinary study in oceanographic- atmospheric science and climate. Here we relate ocean waves to the planet's foremost climate signal – El Nino Southern Oscillation (ENSO). Through detailed analyses of observations, supported by modeling, we use tropical cyclones and wind power as the connecting bridge to explain the inter-relationships between ocean waves, ENSO, wind and tropical cyclones. We furthermore show the potential of using waves or/and wind power as ENSO predictors.